POLITECNICO DI MILANO

Facoltà di Ingegneria Industriale

Corso di Laurea Magistrale in Ingegneria Aeronautica

Linear stability analysis of the asymmetric base flow of two cylinders in side-by-side arrangement

Relatore: Prof. Franco AUTERI
Co-relatore: Dr. Marco CARINI

Tesi di laurea di:
Andrea RIGONI
Matr. 799012

Anno Accademico 2013 - 2014

Abstract

This work is concerned with the numerical investigation of the linear-stability properties of the steady, asymmetric flow past two cylinders in side-by-side arrangement. The problem is governed by two parameters: the Reynolds number and the adimensional gap spacing between the centres of the cylinders. Past works have shown that the eigenvalues, corresponding to the neutral curves which delimit the asimptotically stable region in the parameter space, are sensitive to the length of the computational domain. For this reason, the present study is focused on the research of the minimal domain size, for which the above-mentioned eigenvalues can be considered converged. The present results show that convergence is achieved for a domain length of 550 diameters, even though for certain eigenvalues, a longer length, up to 950 diameters, is required. The analysis is enriched by the calculation of the structural sensitivity to identify the core region of the instability. Then, the neutral curves which delimit the asymptotically stable area are tracked using different domain lengths. In particular, domain lengths of 550 and 950 diameters are employed. The study is completed performing a set of DNSs in strategical points of the parameter space (g, Re) in order to validate the results obtained by the linear stability analysis. The flow is modelled using the Navier–Stokes equations and it is assumed incompressible and steady. The equations are linearised to perform the linear stability analysis in the parameter space. The numerical investigation is performed using a software package written in CPL language and the equations are discretized using the immersed bounday method.

Keywords: Cylinders in side-by-side arrangement, Asymmetric base flow, Linear stability, Structural sensitivity, Neutral curves, Navier–Stokes equations.

Sommario

Questo lavoro concerne l'analisi di stabilità lineare del flusso base asimmetrico attorno ad una coppia di cilindri affiancati immersi in una corrente fluida uniforme. Il problema è governato da due parametri: il numero di Reynolds e la distanza tra i centri dei due cilindri. È stato mostrato in passato come gli autovalori relativi alle curve neutre che delimitano la zona asintoticamente stabile dello spazio dei parametri siano sensibili alla lunghezza del dominio di calcolo. Di conseguenza l'indagine è concentrata sulla ricerca della lunghezza ottimale del dominio, rispetto alla quale i suddetti autovalori convergono. In particolare, i risultati mostrano come, per alcuni autovalori, la convergenza si raggiunge per lunghezze del dominio di calcolo comprese tra 550 e 950 diametri. L'analisi è arricchita dal calcolo della sensitività strutturale in modo da localizzare la zona maggiormente sensibile a una retroazione localizzata della velocità. Successivamente sono stati tracciati i rami delle curve neutre che delimitano l'area stabile nello spazio dei parametri utilizzando due domini di lunghezza differente, a seconda della curva neutra considerata. In particolare sono state impiegate le lunghezze $Lx = 550$ e $Lx = 950$. Lo studio è completato da una serie di DNS in punti strategici in modo da validare quanto ottenuto dall'analisi di stabilità lineare. Il fluido è modellato dalle equazioni di Navier–Stokes sotto le ipotesi di stazionarietà e incomprimibilità. Per effettuare l'analisi di stabilità lineare, le equazioni vengono linearizzate nel punto di interesse all'interno dello spazio dei parametri (g, Re). L'indagine numerica viene effettuata con l'utilizzo di un pacchetto di programmi scritti in linguaggio CPL e le equazioni vengono discretizzate utilizzando il metodo dei corpi immersi.

Parole chiave: Cilindri affiancati, Flusso base asimmetrico, Stabilità lineare, Sensitività strutturale, Curve neutre, Equazioni di Navier–Stokes.

alla mia famiglia,
per avermi dato l'opportunità di vivere
questa fantastica avventura

Ringraziamenti

In questo piccolo spazio del mia tesi, vorrei ringraziare tutte le persone che sono state fondamentali in questo breve, ma intenso, capitolo della mia vita: un pensiero speciale va ai miei genitori e a mio fratello, che tra mille difficoltà e costanti sacrifici mi hanno permesso di raggiungere questo traguardo tanto ambito, non facendomi mai mancare nulla; vi siete sempre dimostrati fiduciosi nelle mie capacità insegnandomi a non mollare mai, anche quando la montagna sembrava troppo alta da scalare. Siete la mia forza e il mio esempio e non dimenticherò mai tutto quello che avete fatto per me.
In secondo luogo vorrei dire grazie a tutti i miei nonni, zii e cugini, per avermi supportato moralmente durante gli esami, per aver gioito e sofferto con me dopo ogni traguardo e per essere stati sempre presenti nelle tappe fondamentali di questo viaggio. Un pensiero speciale va anche tutti quei nonni che mi hanno custodito dall'alto, perché anche se non sono più con me, hanno saputo trasmettermi tante piccole cose, che porto con me nella vita di tutti i giorni.
Un dolce pensiero va anche a Nausicaa, presenza silenziosa e costante che ha riempito la mia vita in un modo che le parole non possono descrivere; grazie per essere sempre stata al mio fianco e per dare un senso ai miei giorni; possa questo lavoro essere l'inizio di tante indimenticabili avventure che avremo la fortuna di vivere assieme.
Grazie di cuore anche a tutti i miei amici, per avermi fatto sentire la loro vicinanza negli ultimi mesi di questo lavoro, in particolare a Mattia e Martina, perché mi hanno dimostrato che l'amicizia che ci lega va al di là delle semplici parole.
Infine vorrei esprimere la mia riconoscienza verso il Prof. F. Auteri, per essere stato, oltre che un ottimo insegnante, anche un valido consigliere, avendo sempre a cuore il conseguimento di questo mio importante traguardo, soprattutto quando le cose sembravano non funzionare. Mi ha fatto innamorare della fluidodinamica e ha messo a disposizione tutte le sue competenze e la sua pazienza per rendere questo lavoro il più speciale possibile.
Ringrazio inoltre il mio correlatore Marco Carini, per l'immensa disponibilità mostrata in questi mesi, attaverso messaggi di posta quotidiani e lunghe telefonate notturne.
Un riconoscimento va anche al Politecnico di Milano e al Prof. F. Giannetti dell'Università

di Salerno per le numerose risorse di calcolo messe a mia disposizione durante questi mesi e senza le quali questo studio non sarebbe stato possibile.
Ringrazio infine te, che stai leggendo questo mio piccolo lavoro, perchè la curiosità che ti ha spinto a sfogliare queste pagine possa esserti utile per capire come, grazie all'ingegneria, riusciamo a capire un po' più a fondo questo fantastico mondo in cui viviamo.

Contents

Introduction

(a) *The Golden Gate Bridge on the San Francisco Bay.*

(b) *The Petronas Towers in Kuala Lumpur.*

(c) *Chimneys in a nuclear powerplant.*

Figure 0.1: *Example of buildings whose structure is made by two bluff bodies in side-by side arrangement*

The simulation of the viscous flow over a bluff body has been a challenging problem for several years. Such flows are of great interest because they show fundamental fluid dynamic phenomena, including separated shear layers and turbulence. Many structures such as tall buildings, bridges, off-shore pipelines and risers may be considered as bluff bodies and the complex flow over them is of great interest. In addition, some streamlined structures may behave as a bluff body at some operating conditions, such as an airplane

wing at high angles of attack. Among the different bluff-body shapes, the circular section has received considerable attention by researchers. This is due to several reasons:

- it is widely used in many practical applications, such as pipelines and heat exchanger tubes, twin struts to support biplane wings in aeronautical engineering, or in tall buildings and in the towers of suspension bridges in wind engineering;
- the circular cylinder is a simple geometry for analysis and simulations;
- the flow over a circular cylinder encompasses all the important aspects of bluff body flow, making this shape the prototype of bluff body *par excellence*.

When more than one cylinder is placed in a fluid stream, several changes in the characteristics of fluid loads occur due to the interference effect: for instance, the wake interaction between the two bodies can affect considerably the forces acting on them, with respect to a single-body flow. In particular, the flow past two cylinders in side-by-side arrangement has been one of the most studied problems in fluid mechanics since 1977 with the work of Zdravkovich who analized not only this configuration but also the in-tandem and staggered arrangements; in fact, even though the geometry is quite simple, the phenomena that characterise this problem are complicated, making quite difficult understanding the whole scenario from a physical and an engineering point of view.
The present investigation is limited to the case of a viscous, laminar, incompressible flow past two side-by-side cylinders. The problem can be described by two nondimensional parameters, the Reynolds number and the gap spacing, as reported in Table 0.1.:

$Re = \frac{UD}{\nu}$	U = velocity vector D = cylinder diameter ν = kinematic viscosity
$g = \frac{L}{D}$	L = distance between the two cylinders D = cylinder diameter

Table 0.1: *Governing parameters for two cylinders in side-by-side arrangement.*

Different patterns have been observed in both experimental and numerical works. For instance, in a wind and water tunnel test campaign Xu et al. (2003) investigated the effect of the Reynolds number, in the range $150 - 14.300$, and of the nondimensional gap size on the flow structure behind two side-by-side cylinders. Three main patterns have been observed: for $g < 1.25$, the two cylinders act like a single bluff body, generating a single vortex street; for $1.25 < g < 1.6$ two flow structures have been observed: for low Re, a single vortex street is created, fluctuating with a nondimensional frequency $f \approx 0.09$. Increasing the Reynolds number, two wakes are formed, a narrow one and a wide one. The two vortex streets are associated with a dominant frequency of about 0.3 and 0.09, respectively. Finally, for $1.6 < g < 2.0$, the single vortex street is no more observed and the flow consists of one narrow and one wide street. It is further observed

that the critical Re, at which the transition from single to double street occurs, increases as g decreases.
An interesting numerical study has been carried out by Kang in 2003. Six different flow patterns (antiphase-synchronized, in-phase synchronized, flip-flopping, deflected, single-bluff-body, and steady wake) have been discovered in the ranges of $40 \leq Re \leq 160$ and $g < 5$. In his work, Kang also showed how the vortex-shedding frequency strongly depends on the gap spacing and how this affects the values of the lift and drag coefficient. In particular, when decreasing g in the flip-flopping regime, first the frequency drastically goes down and then slightly increases when the single bluff-body pattern is established. A detailed map of the dependence of the wake pattern on Re and g has also been obtained showing that each pattern occupies a finite area in the parameter space.
Further studies have been performed to analyse the linear stability of the flow. Akinagawa & Mizushima (2005) investigated the linear stability of the flow past two cylinders in side-by-side arrangement theoretically, numerically and experimentally, in order to explore the origin of the in-phase and antiphase oscillatory flows. The authors found that these two patterns are related to the presence of two modes which become unstable and calculated the corresponding critical Reynolds number Re_c and nondimensional frequency (*i.e.* the Strouhal number) for different gap values.
In 2008, Mizushima & Ino presented a more detailed work, exploiting numerical and analytical techniques to better investigate the development of the different flow patterns, varying the Reynolds number and the gap between the two cylinders. Despite the mechanism that produced every single pattern was not clear, the stability analysis revealed that the insurgence of the different flow patterns is related to the presence of two unstable modes. The first one is symmetric and becomes unstable for $Re = 40.72$ while the second one is asymmetric and becomes unstable for $Re = 52.36$, both for g = 4. The critical values of the Reynolds number change when the gap is reduced to $g = 1$, becoming $Re = 42.24$ for the symmetric one and $Re = 45.34$ for the asymmetric one.
In the last few years, many investigations have been carried out to understand where the core of the instability is located in the domain, employing the structural-sensitivity-analysis technique proposed by Giannetti & Luchini in 2007. In particular, the instability core, or "wavemaker", is located where the product of the direct and adjoint modes is maximum. The origin of the flip-flop behaviour has been investigated by Carini, Giannetti & Auteri (2014) in the range of non-dimensional gap spacing $0.6 < g < 1.4$ and Reynolds number $50 < Re \leq 90$. In this work, the authors explain how, starting from the in-phase synchronized vortex shedding, the flip-flop pattern occurs when a pair of complex-conjugate Floquet exponents becomes unstable, crossing the imaginary axis. Starting from the critical threshold of $g = 0.7$, $Re = 61.74$, the stability analysis has been extended to cover an entire range of gap spacing; this leads to the possibility of drawing the neutral curves (*i.e* the curves in the parameter space on which a specific eigenvalue has null real part); furthermore, the sensitivity map of the flip-flop pattern has been calculated showing that the instability core is located in the wake behind the two cylinders.
In another contribution, Carini, Giannetti & Auteri (2014) examined the global stabil-

ity of the symmetric base flow in the parameter range of $0.1 \leq g \leq 3$ and $Re < 100$. Four different unstable modes are found, each one promoting a different kind of unstable pattern as the gap spacing g is varied: single bluff body, asymmetric, in-phase and antiphase synchronized vortex shedding. For each instability pattern the neutral curves are calculated in the parameter space (Re, g) in order to identify the regions of stability and instability of the corresponding base flow. Moreover, the structural-sensitivity map related to each mode is depicted, in order to identify the region where the instability core is located. Finally, the stuctural sensitivity analysis of the in-phase and antiphase mode has been employed to design a passive control of these unstable modes for $g = 2.5$ and $Re = 60$.
Taking into account the above results, this work is focused on the numerical study of the steady asymmetric base flow region represented in blue in Figure 0.2.

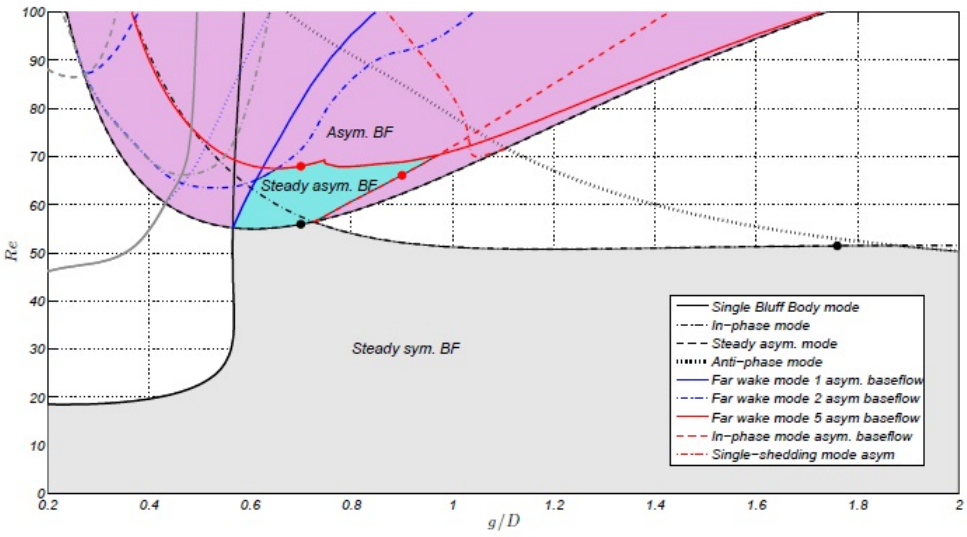

Figure 0.2: *Neutral curves in the $g - Re$ plane, for a domain length equal to $L_x = 125$ cylinder diameters.*

The investigation of this region is interesting because the asymmetric base flow has not been studied yet and therefore the region in which this pattern is asymptotically stable is not well defined. A previous, inconclusive study [10] has shown that an unstable eigenvalue, which has an imaginary part of $\mu = 0.39i$, represented in Figure 0.2, by the red neutral curve is very sensitive to the domain length. This means that extending the computational domain in the x direction may change significantly the real and the imaginary part of the unstable eigenvalue. Starting from this issue, the objectives of this analysis are two: the first is to find the most suitable domain length for the stability analysis of two cylinders in side by side arrangement, *i.e.* the lenght for which the most unstable eigenvalue becomes insensitive to the domain length. The second is to re-define the area, coloured in blue in Figure 0.2, where the steady, asymmetric base flow is stable

by, tracking the neutral curves for the extended domain length.
The thesis is organised as follows: in Chapter 1 the mathematical formulation of the problem is presented and the main mathematical tools used for this analysis are described. Chapter 2 contains a validation of all of the pieces of software used during the analysis, through the simulation of the flow past a singular cylinder. In Chapter 3 the main results of the present work are reported. Conclusions are presented in Chapter 4.

CHAPTER 1

Problem formulation

In this chapter, an overview of the main concepts and tools used in this work is presented. In particular, the theory of nonlinear dynamical systems and their linearisation are described. The aim is to give the reader both an essential but complete summary of the concepts necessary to understand the entire work and the opportunity to approach these theories from a wider point of view.
Nonlinearities are ubiquitous in physical phenomena: for instance gas dynamics, combustion and fluid mechanics are all governed by nonlinear equations. In addition, since the nonlinear systems are difficult to analyse, it is useful to develop a set of reliable methods to investigate them, in order to better understand the physics underlying the different phenomena that we examine.

1.1 Nonlinear dynamical systems

A dynamical system is a set of Ordinary Differential Equations (ODEs) or Partial Differential Equations (PDEs) which describes the evolution in time of a set of quantities, *i.e.*

$$\begin{cases} \dfrac{\partial \mathbf{x}(\mathbf{r},t)}{\partial t} = \mathcal{F}(\mathbf{x}(\mathbf{r},t),\boldsymbol{\lambda}), \\ \mathbf{x}(\mathbf{r},0) = \mathbf{x}_0(\mathbf{r}), \end{cases} \tag{1.1}$$

where $\mathbf{x}(\mathbf{r},t)$ denotes the state vector and belongs to the *phase (or state) space* $\mathcal{H}$ ($\mathcal{H} \subset \mathbb{R}^d, d \in \mathbb{N}$ in the case of finite dimension spaces), $\mathbf{x}_0(\mathbf{r})$ denotes the initial condition, $\mathbf{r}$ is the position vector and t represents the time variable ($t \in T$ where T is the *time set*); $\mathcal{F}$ is a *family of evolution operators* that maps $\mathcal{H}$ into itself and satisfies the following semigroup properties:

$$\int_0^0 \mathcal{F}(\tau)\, d\tau = \mathcal{I}, \tag{1.2}$$

$$\int_t^{t+s} \mathcal{F}(\tau)\, d\tau = \mathcal{F}(t) \circ \mathcal{F}(s). \tag{1.3}$$

The vector $\boldsymbol{\lambda}$ represents a vector of parameters which affect the behaviour of the nonlinear system. For instance, in the case of two cylinders in side-by-side arrangement, $\boldsymbol{\lambda}$ has the following components: $\boldsymbol{\lambda} = \begin{bmatrix} g & Re \end{bmatrix}^T$ where g denotes the non-dimensional gap spacing between the two cylinders and Re represents the Reynolds number. This means that, varying the gap spacing and the Reynolds number, different patterns may be observed in the case of two side-by-side cylinders.
A nonlinear dynamical system may have an arbitrary number of solutions, which depend on the different initial conditions and on the values assumed by $\boldsymbol{\lambda}$. For this reason, starting from different $\mathbf{x}_0$ and $\boldsymbol{\lambda}$, different solutions of the state $\mathbf{x}(t)$ may be reached in the long term. In particular, interesting solutions of (1.1) are the so-called *steady states*, *i.e.* those solutions which satisfy the following relation:

$$\begin{cases} \mathcal{F}(\mathbf{x}_s(\mathbf{r}), \boldsymbol{\lambda}) = 0, \\ \mathbf{x}(\mathbf{r}, 0) = \mathbf{x}_0(\mathbf{r}), \end{cases} \tag{1.4}$$

where the subscript s stands for *steady*.
These particular states are very interesting from a physical point of view, because they represent equilibrium solutions: in fact, since the time-derivative is null, the state vector $\mathbf{x}_s(\mathbf{r})$ does not change in time when the steady state is assumed as initial condition (for this reason the solutions of (1.4) are often called *fixed points*). From an engineering perspective, the study of the steady states of a dynamical system is fundamental, since we are interested in the long-time, *i.e.* for $t \to \infty$, behaviour of the solution; in fact, many processes in nature reach the regime condition after a transient phase.

1.1.1 The Navier–Stokes equations

This work is concerned with the stability of the incompressible flow around two bluff bodies, the dynamical system is therefore described by the Navier–Stokes equations. These equations describe the motion of a Newtonian fluid

$$\begin{cases} \dfrac{\partial \mathbf{u}^*}{\partial t} + (\mathbf{u}^* \cdot \nabla)\mathbf{u}^* - \nu \nabla^2 \mathbf{u}^* + \nabla p^* = \mathbf{f}, \\ \nabla \cdot \mathbf{u}^* = 0, \end{cases} \tag{1.5}$$

where $\mathbf{u}^* = \mathbf{u}^*(\mathbf{r}, t)$ denotes the velocity vector, $p^* = p^*(\mathbf{r}, t)$ represents the reduced pressure, $\mathbf{f} = \mathbf{f}(\mathbf{r})$ is a vector of external forces acting on the fluid and ν denotes the kinematic viscosity.
In the analyses that follow, we will consider a fluid-dynamic system without external

forces, for this reason the term $\mathbf{f}$ will be dropped in the sequel, leading to a homogeneous system.
It is possible to adimensionalise (1.5) introducing a reference velocity U^* and a reference length L^* and defining the nondimensional quantities as

$$\mathbf{u} = \frac{\mathbf{u}^*}{U^*}, \qquad p = \frac{p^*}{P^*}; \tag{1.6}$$

where $P^* \equiv \rho^* U^{*2}$. Then, the adimensional Navier–Stokes equations read:

$$\begin{cases} \dfrac{\partial \mathbf{u}}{\partial t} + (\mathbf{u}\cdot\nabla)\mathbf{u} - \dfrac{1}{Re}\nabla^2\mathbf{u} + \nabla p = 0, \\ \nabla\cdot\mathbf{u} = 0, \end{cases} \tag{1.7}$$

where the Reynolds number is defined as $Re = \frac{U^* L^*}{\nu}$. Therefore, as we may see, one of the parameters that govern the physics of the problem comes from the adimensionalisation. The second one, the nondimensional gap spacing, is not visible in these equations, since it is a geometric parameter, not a fluid-dynamic one.
The system must be completed by boundary and initial conditions:

$$\begin{cases} \dfrac{\partial \mathbf{u}}{\partial t} + (\mathbf{u}\cdot\nabla)\mathbf{u} - \dfrac{1}{Re}\nabla^2\mathbf{u} + \nabla p = 0, \\ \nabla\cdot\mathbf{u} = 0, \\ \mathbf{u}(\mathbf{r},t)|_{\Gamma_D} = 0, \\ \left(\dfrac{1}{2}\nu\left[\nabla\mathbf{u} + (\nabla\mathbf{u})^T\right]\cdot\mathbf{n} - p\mathbf{n}\right)\Big|_{\Gamma_N} = 0, \\ \mathbf{u}(\mathbf{r},0) = \mathbf{u}_0, \end{cases} \tag{1.8}$$

where Γ_D and Γ_N are the Dirichlet boundary and the Neumann boundary, respectively, such that $\Gamma_D \cup \Gamma_N = \partial\Omega$ and $\Gamma_D \cap \Gamma_N = \emptyset$, with $\partial\Omega$ the entire boundary.
The steady states of (1.8) are the pairs $\mathbf{q} = \begin{bmatrix}\mathbf{u} & p\end{bmatrix}^T$ that satisfy the following system:

$$\begin{cases} (\mathbf{u}\cdot\nabla)\mathbf{u} - \dfrac{1}{Re}\nabla^2\mathbf{u} + \nabla p = 0, \\ \nabla\cdot\mathbf{u} = 0, \\ \mathbf{u}(\mathbf{r},t)|_{\Gamma_D} = 0, \\ \left(\dfrac{1}{2}\nu\left[\nabla\mathbf{u} + (\nabla\mathbf{u})^T\right]\cdot\hat{\mathbf{n}} - p\hat{\mathbf{n}}\right)\Big|_{\Gamma_N} = 0. \end{cases} \tag{1.9}$$

As we may note, the unsteady term *i.e.* the derivative with respect to time of $\mathbf{u}$ has been dropped. The two fields $\mathbf{U} = \mathbf{U}(\mathbf{r})$ and $P = P(\mathbf{r})$, which represent the solution of (1.9), are also called *base flow*. The calculation of the base flow is the first step in a linear stability analysis. It is worthwhile to remark that different base flows may exist depending on the parameters (Re, g). In particular, for the problem studied in this work, beside the asymmetric base flow, a symmetric base flow also exists whose stability properties have been studied in detail in [10].

1.1.2 Newton's Method

The first step in a linear stability analysis is to find the fixed points of the nonlinear system. While there are several methods able to compute the solution of nonlinear systems of equations, Newton's method is one of the most employed due to its high efficiency and accuracy. Moreover, it allows to compute unstable fixed points, that would be out of reach for time-stepping procedures.
The Newton's method can be applied to a nonlinear system to calculate the solutions of (1.4). Expanding $\mathcal{F}(\mathbf{x})$ in a Taylor series in the neighbourhood of an approximate solution $\mathbf{x}_{n+1}$ at the $(n+1)-th$ step, and by truncating the series to first order, we obtain:

$$\mathcal{F}(\mathbf{x}_{n+1},\lambda) \approx \mathcal{F}(\mathbf{x}_n,\lambda) + \mathbf{J}(\mathbf{x}_n,\lambda)(\mathbf{x}_{n+1}-\mathbf{x}_n). \tag{1.10}$$

Because of (1.4), (1.10) becomes:

$$\mathcal{F}(\mathbf{x}_n,\lambda) + \mathbf{J}(\mathbf{x}_n,\lambda)(\mathbf{x}_{n+1}-\mathbf{x}_n) = 0; \tag{1.11}$$

from this equation the approximate solution $\mathbf{x}_{n+1}$ can be computed. The procedure is repeated until convergence.
In the case of the Navier–Stokes equations, the variable $\mathbf{x}$ and the paramater λ can be expressed as

$$\mathbf{x} = \begin{pmatrix}\mathbf{u} & p\end{pmatrix}^T, \qquad \lambda = Re, \tag{1.12}$$

while the term $\mathcal{F}(\mathbf{x},\lambda)$ can be written as

$$\mathcal{F}(\mathbf{x},\lambda) = \mathcal{Q}(\mathbf{x},\mathbf{x}) + \mathcal{L}(\mathbf{x},\lambda) \tag{1.13}$$

where the term $\mathcal{Q}(\mathbf{x},\mathbf{x})$ is a bilinear quadratic form and $\mathcal{L}(\mathbf{x},\mathbf{x})$ is a linear form

$$\mathcal{Q}(\mathbf{x},\mathbf{y}) = \begin{pmatrix}(\mathbf{u}\cdot\nabla)\mathbf{v}\\ 0\end{pmatrix}, \qquad \mathcal{L}(\mathbf{x},\lambda) = \begin{pmatrix}-\frac{1}{Re}\nabla^2\mathbf{u} + \nabla p\\ \nabla\cdot\mathbf{u}\end{pmatrix}, \tag{1.14}$$

while the Jacobian Matrix can be expressed as:

$$\mathbf{J}(\mathbf{v},Re) = \begin{bmatrix}(\mathbf{v}\cdot\nabla)\cdots + (\cdots\cdot\nabla)\mathbf{v} - \frac{1}{Re}\nabla^2\cdots & \nabla\ldots\\ \nabla\cdot\ldots & 0\end{bmatrix}. \tag{1.15}$$

1.2 Linear stability

In order to investigate the stability properties of a fixed point (base flow), the simplest and most valuable tool is linear stability analysis. This means to study dynamical properties of the linearised problem in the neighbourhood of a steady state and gives us information about the behaviour of system subject to infinitesimally small perturbations. In particular, in this work, the linear-stability approach is used to determine whether the base flow calculated in the previous section, in this work in particular the asymmetric

base flow, is stable or unstable for a fixed value of g and Re. Let us briefly recall now the steps of this approach:

1. a fixed point, or base flow when the dynamical system is modelled by the Navier–Stokes equations, of the nonlinear system is calculated, *i.e.* one of the solutions $\mathbf{x}_{si}$ of (1.4) is found;

2. the system is linearised around the fixed point. The discrete, linearised system will read:

$$\mathbf{M}\frac{d\mathbf{x}}{dt} = \mathbf{A}\mathbf{x} \tag{1.16}$$

   where $\mathbf{x}$ is the state vector, $\mathbf{M}$ is the mass matrix and $\mathbf{A}$ is the *Jacobian matrix* calculated in the fixed point $\mathbf{x}_{si}$ of the system (1.1) whose stability is being investigated, thus:

$$\mathbf{A} = \left.\frac{\partial \mathcal{F}}{\partial \mathbf{x}}\right|_{\mathbf{x}_{si}} = \left.\frac{\partial \mathcal{F}_j}{\partial x_k}\right|_{\mathbf{x}_{si}}; \tag{1.17}$$

3. The eigenvalues of $\mathbf{A}$ are computed and the linear stability of the system is deduced exploiting two theorems:

   Theorem 1. *(see e.g. [24]) Let $\boldsymbol{x}_{si}$ be a fixed point of* (1.1)*. If all of the eigenvalues of the matrix $\boldsymbol{A}$ have strictly negative real part then $\boldsymbol{x}_{si}$ is an asympotically stable equilibrium point for the system* (1.1)*.*

   Theorem 2. *(see e.g. [24]) Let $\boldsymbol{x}_{si}$ be a fixed point of* (1.1)*. If the matrix $\boldsymbol{A}$ has at least one eigenvalue with strictly positive real part then $\boldsymbol{x}_{si}$ is an unstable equilibrium point for both the nonlinear system* (1.1) *and linearised system* (1.16)*.*

Such an approach gives us information about the behaviour of the system in a vanishing neighbourhood of the fixed point. For a deeper understanding of the flow behaviour subject to finite-energy perturbations, a nonlinear analysis is required.

1.2.1 Linearised Navier–Stokes equations (LNSE)

The procedure to obtain the linearised equations for an incompressible, uniform-density flow starting from the Navier–Stokes equations is recalled in this section for reader's convenience. For the sake of brevity, only the main steps will be considered.
To linearise (1.5), let us express the velocity vector $\mathbf{u}$ and the pressure p as the sum of a steady solution, the base flow, and a small perturbation term, namely: $\mathbf{u} = \mathbf{U} + \mathbf{u}'$ and $p = P + p'$ and then introduce these expressions in (1.7). We obtain

$$\begin{cases} \dfrac{\partial(\mathbf{U} + \mathbf{u}')}{\partial t} + ((\mathbf{U} + \mathbf{u}') \cdot \nabla)(\mathbf{U} + \mathbf{u}') - \dfrac{1}{Re}\nabla^2(\mathbf{U} + \mathbf{u})' + \nabla(P + p') = 0, \\ \nabla \cdot (\mathbf{U} + \mathbf{u}') = 0. \end{cases} \tag{1.18}$$

Recalling the linearity of the derivative operator and neglecting the second-order term, the *linearised Navier–Stokes equations* are obtained:

$$\begin{cases} \dfrac{\partial \mathbf{u}'}{\partial t} + (\mathbf{U}\cdot\nabla)\mathbf{u}' + (\mathbf{u}'\cdot\nabla)\mathbf{U} - \dfrac{1}{Re}\nabla^2\mathbf{u}' + \nabla p' = 0, \\ \nabla\cdot\mathbf{u}' = 0, \\ \mathbf{u}'(\mathbf{r},t)\big|_{\Gamma_D} = 0, \\ \left(\dfrac{1}{2}\nu\big[\nabla\mathbf{u}' + (\nabla\mathbf{u}')^T\big]\cdot\hat{\mathbf{n}} - p\hat{\mathbf{n}}\right)\Big|_{\Gamma_N} = 0, \\ \mathbf{u}'(\mathbf{r},0) = \mathbf{u}_0, \end{cases} \tag{1.19}$$

where the Jacobian operator $\mathbf{A}$ has the form:

$$\mathbf{A} = \begin{bmatrix} (\mathbf{U}\cdot\nabla)\cdots + (\cdots\nabla)\mathbf{U} - \frac{1}{Re}\nabla^2\ldots & \nabla\ldots \\ \nabla\cdot\ldots & 0 \end{bmatrix}. \tag{1.20}$$

1.2.2 Direct and adjoint problem

To compute the eigenvalues and the eigenvectors associated with (1.19) the solution has to be expressed in the form:

$$\mathbf{u}'(\mathbf{r},t) = \hat{\mathbf{u}}(\mathbf{r})e^{\lambda t}, \qquad p'(\mathbf{r},t) = \hat{p}(\mathbf{r})e^{\lambda t}, \tag{1.21}$$

where λ is the generic eigenvalue and $\hat{\mathbf{q}} = \begin{bmatrix}\hat{\mathbf{u}} & \hat{p}\end{bmatrix}^T$ is the corresponding eigenvector. Substituting it into (1.19), the sytem can be written as

$$\begin{cases} \lambda\mathbf{u}' + (\mathbf{U}\cdot\nabla)\mathbf{u}' + (\mathbf{u}'\cdot\nabla)\mathbf{U} - \dfrac{1}{Re}\nabla^2\mathbf{u}' + \nabla p' = 0, \\ \nabla\cdot\mathbf{u}' = 0, \\ \mathbf{u}'(\mathbf{r},t)\big|_{\Gamma_D} = 0, \\ \left(\dfrac{1}{2}\nu\big[\nabla\mathbf{u}' + (\nabla\mathbf{u}')^T\big]\cdot\hat{\mathbf{n}} - p\hat{\mathbf{n}}\right)\Big|_{\Gamma_N} = 0, \\ \mathbf{u}'(\mathbf{r},0) = \mathbf{u}_0, \end{cases} \tag{1.22}$$

or, in the discrete form:

$$\lambda\mathbf{M}\hat{\mathbf{q}} = \mathbf{A}\hat{\mathbf{q}}. \tag{1.23}$$

Beside the direct problem,it is useful to introduce the adjoint problem [26]: it can be obtained by multiplying both sides of the momentum equation by a vector function $\mathbf{v} = \mathbf{v}(\mathbf{r},t)$, and the incompressibily constraint by a scalar function $m = m(\mathbf{r},t)$. After integrating by parts, the adjoint problem can be stated as:

$$\begin{cases} -\dfrac{\partial \mathbf{v}}{\partial t} - (\mathbf{U}\cdot\nabla)\mathbf{v} + (\nabla\mathbf{U})\mathbf{v} - \dfrac{1}{Re}\nabla^2\mathbf{v} + \nabla m = 0, \\ \nabla\cdot\mathbf{v} = 0, \\ \mathbf{v}(\mathbf{r},t)|_{\Gamma_D} = 0, \\ \left(\dfrac{1}{2}\nu\big[\nabla\mathbf{v} + (\nabla\mathbf{v})^T\big]\cdot\hat{\mathbf{n}} - m\hat{\mathbf{n}}\right)\Big|_{\Gamma_N} = 0, \\ \mathbf{v}(\mathbf{r},0) = \mathbf{v}_0. \end{cases} \tag{1.24}$$

Also in this case, the eigenvalues and eigenvectors can be computed writing the variables $\mathbf{v}(\mathbf{r},t)$ and $m((\mathbf{r},t)$ as:

$$\mathbf{v}(\mathbf{r},t) = \hat{\mathbf{v}}(\mathbf{r})e^{-\lambda t} \qquad m(\mathbf{r},t) = \hat{m}(\mathbf{r})e^{-\lambda t}; \tag{1.25}$$

therefore the adjoint eigenvalue problem reads:

$$\begin{cases} \lambda\hat{\mathbf{v}} - (\mathbf{U}\cdot\nabla)\hat{\mathbf{v}} + (\nabla\mathbf{U})\hat{\mathbf{v}} - \dfrac{1}{Re}\nabla^2\hat{\mathbf{v}} + \nabla\hat{m} = 0, \\ \nabla\cdot\hat{\mathbf{v}} = 0, \\ \hat{\mathbf{v}}(\mathbf{r},t)|_{\Gamma_D} = 0, \\ \left(\dfrac{1}{2}\nu\big[\nabla\hat{\mathbf{v}} + (\nabla\hat{\mathbf{v}})^T\big]\cdot\hat{\mathbf{n}} - m\hat{\mathbf{n}}\right)\Big|_{\Gamma_N} = 0, \end{cases} \tag{1.26}$$

or, in discrete form:

$$\lambda^*\mathbf{M}\hat{\mathbf{q}}^+ = \mathbf{A}^+\hat{\mathbf{q}}^+, \tag{1.27}$$

where the vector $\hat{\mathbf{q}}^+$ represents the adjoint eigenvector, *i.e.* $\hat{\mathbf{q}}^+ = \begin{bmatrix}\hat{\mathbf{v}} & \hat{m}\end{bmatrix}$ and λ^* is the complex conjugate of λ. It is important to underline that the direct and adjoint eigenvalues are the same, while the adjoint eigenvectors are different from the direct ones. In particular, the adjoint eigenvectors are also called left eigenvectors since they are the eigenfunctions of $\mathbf{A}^+ = \mathbf{A}^H$ for a discrete system.

1.2.3 Arnoldi's algorithm

In this section the Arnoldi's algorithm for the computation of the eigenvalues is described. Before illustrating this method it is useful to recall some basic notions about the Krylov subspaces. A *Krylov subspace* is a vector subspace, which can be written in the form:

$$\mathcal{K}_k(\mathbf{A},\mathbf{v}) = \begin{bmatrix}\mathbf{v}_0 & \mathbf{A}\mathbf{v}_0 & \mathbf{A}^2\mathbf{v}_0 & \dots & \mathbf{A}^{k-1}\mathbf{v}_0,\end{bmatrix} \qquad \mathbf{v}\in\mathbb{C}^{n\times n}, \tag{1.28}$$

where $\mathbf{A}$ represents a generic matrix. A fundamental property is that $\mathcal{K}_k$ is the subspace of all vectors in $\mathbb{R}^n$ which can be written as $x = p(A)v$, where p is a polynomial of degree not exceeding $k-1$.
Krylov subspaces are exploited by *Arnoldi's Algorithm*, that is an iterative projection method, which project a general non-Hermitian matrix onto a Krylov subspace, thus it

provides the computation of an orthogonal basis for $\mathcal{K}_k$. It is presented in this work because it is useful to approximate the eigenvalues of large sparce matrices. In fact, large-scale eigenvalue problems are ubiquitous in engineering and they typically derive from applications in which one is only interested in a small subset of the spectrum, for instance the smallest-or the largest-magnitude eigenvalues. Given a matrix $\mathbf{A} \in \mathbb{R}^{n \times n}$ its eigenvalues can be computed by projecting $\mathbf{A}$ in a low-dimensional subspace and then solving a small eigenvalue problem. The small portion of the spectrum computed is an accurate approximation to the corresponding eigenvalues of the original matrix. The methods which are based on this idea are called *projection methods*.
Arnoldi's Algorithm can be summarized as follows:

1. Choose an arbitrary vector v_1, such that $||v_1||_2 = 1$
2. For $j = 1, 2, ..., k$ Do:
3. Compute $h_{ij} = (\mathbf{A}v_j, v_i)$ for $i = 1, 2, ..., j$
4. Compute $w_j = \mathbf{A}v_j - \sum_{i=1}^{j} h_{ij} v_i$
5. $h_{j+1,j} = ||w_j||_2$
6. If $h_{j+1,j} = 0$ then Stop
7. $v_{j+1} = w_j / h_{j+1,j}$
8. EndDo

Two sets of quantities are computed by this procedure: the first one are the nonzero entries h_{ij} of the Hessenberg matrix $\mathbf{H}$. The second one is the set of vectors v_1, v_2, ..., v_k which represent the columns of the matrix $\mathbf{V}_k$.
The lines 4, 5 and 7 of the algorithm can be summarized in the formula:

$$\mathbf{A}\mathbf{v}_j = \sum_{i=1}^{j+1} h_{ij} v_i \quad j = 1, 2, ..., k. \tag{1.29}$$

The equation can be written in its matrix form; recalling the property that $\mathbf{V}_k^{-1} = \mathbf{V}_k^H$ since it is an orthogonal matrix, the matrix form of (1.29) reads:

$$\mathbf{V}_k^H \mathbf{A} \mathbf{V}_k = \mathbf{H} \tag{1.30}$$

(1.30) represents a reduced eigenvalue problem where $\mathbf{H}$ contains a small portion of the spectrum of the matrix $\mathbf{A}$.
In the present work, the "implicitly restarted Arnoldi algorithm" implemented in the ARPACK library with a shift-invert strategy has been used.

1.2.4 Continuation of the solution

The study of the stability properties in a wide region of the parameter space requires a big computational effort: in fact the computation of the different quantities useful to

perform the linear stability analysis is onerous and slow. To overcome this problem, a continuation algorithm is required to automate the analysis in each point of the (Re, g) parameter space. In particular, in the present work, the continuation algorithm has been employed to track the different Hopf bifurcations, to reconstruct the neutral curves which delimit the stability area of the asymmetric base flow. Starting from a point close enough to the neutral curve, the algorithm is able to track it, computing only the eigenvalue of interest, thus avoiding the computation of a spectrum portion at each point.
The different continuation algorithms which have been used are included in the open-source Library Of Continuation Algorithms (LOCA) freely avaiable online. A list of the algorithms provided with the library is reported below:

1. ZERO_ORDER_CONTINUATION
2. FIRST_ORDER_CONTINUATION
3. ARC_LENGTH_CONTINUATION
4. TURNING_POINT_CONTINUATION
5. PITCHFORK_CONTINUATION
6. HOPF_CONTINUATION

In particular, a zero-order continuation of the fixed point has been used to locate the neutral curve in the (Re, g) parameter space; once the neutral curve has been located, a Hopf-bifurcation continuation has been exploited to track the neutral curves delimiting the asymptotically stable region of the asymmetric base flow.
For further information and details about how these algorithms work, the reader is referred to the LOCA manual [23].

1.3 Structural sensitivity

The structural-sensitivity analysis is a relatively new technique, first proposed in 2007 by Giannetti and Luchini [6], and represents a powerful method to locate the core of an absolute instability, also called "wavemaker". Starting from the direct and adjoint eigenvectors, this can be done by computing the structural sensitivity parameter, defined as

$$s(\mathbf{r}) = \frac{||\hat{\mathbf{v}}_i(\mathbf{r})||\ ||\hat{\mathbf{u}}_i(\mathbf{r})||}{\int_\Omega \hat{\mathbf{v}}_i \cdot \hat{\mathbf{u}}_i} \tag{1.31}$$

where $\mathbf{u}_i(\mathbf{r})$ and $\mathbf{v}_i(\mathbf{r})$ represent the *i-th* direct and adjoint eigenvector respectively associated with the least stable eigenvalue. The maxima of this function represent the regions where a localized velocity feedback is able to produce the largest drift of the least stable eigenvalue because it is located in the region where the instability mechanism acts.
Heuristically speaking, what motivates the simultaneous usage of both the direct and

adjoint modes is that for highly non-normal systems, the spatial distribution of direct and adjoint eigensolutions is different: for this reason the wavemaker cannot be identifed from the study of the direct and adjoint eigenfunctions separately.
To write $s(\mathbf{r})$ in its final form, as reported in (1.31), the knowlegde of the base flow $\mathbf{S} = (\mathbf{U}, P)$ is required. A perturbation to the base flow is introduced, modifying the least stable eigenvalue and the correspondent eigenvector. Then, a perturbed eigenvalue problem can be written; after a few mathematical manipulations and exploiting the adjoint problem, the structural sensitivity parameter can be written in its final form. For more details on the necessary algebraic manipulations, see [6].

1.4 Immersed boundary method

In this work, the nonlinear and linearised Navier–Stokes equations have been discretised by a second order finite difference scheme. An "immersed boundary" technique has been employed to deal with the solid bodies in the flow-field. In this approach the bodies in the flow field are simulated by adding a force term in the equations which allows the boundary conditions on the immersed boundary to be imposed. As a consequence the discretization grid occupies the whole domain as depicted in Figure 1.1.

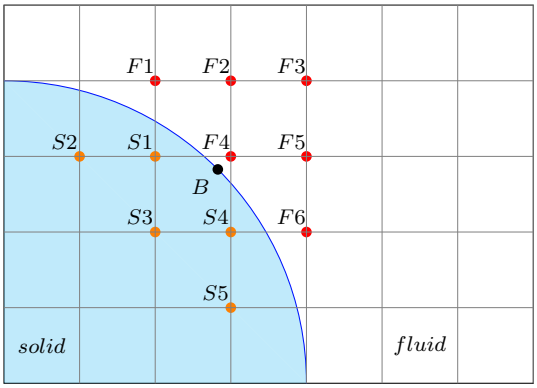

Figure 1.1: *Example of computational domain discretized with a uniform grid using the immersed boundary technique. The boundary conditions imposed by the presence of the cylinder are simulated introducing a forcing term into the governing equations. The points $F1$ to $F6$ and $S1$ to $S5$ are employed to impose the boundary conditions in the point B.*

As anticipated, to take the presence of the body into account a forcing term must be added to the equations. This force must reproduce the same effects produced by the body on the pressure and velocity distributions. Since we are introducing a right hand side in the equations, the homogeneous problem described by (1.9) becomes a forced problem with a vector force field $\mathbf{f}_b = \begin{bmatrix} \mathbf{f}_q & f_m \end{bmatrix}^T$ where the first component is applied to the momentum equation, the second to the incompressibility constraint. There are mainly two ways to introduce the forcing term into the equations: a continuous approach

and a discrete approach. In the former, $\mathbf{f}_b$ is incorporated in the continuous equations, while in the latter the forcing term is applied to the discretised equations. A strong point of the continuous forcing approach is that it is formulated independently of the spatial discretization. On the other hand, the discrete forcing approach depends very much on the discretization method. However, this allows direct control over the numerical accuracy and stability properties of the solver.
The boundary conditions on the body surface (point B in Figure 1.1) can be imposed by an interpolation of the variables using the points in the neighbourhood of the surface. Interpolations of different orders can be used (linear, bilinear, quadratic, ect.) and many interpolation techniques have been used in the past (see [15], [16], [17], [18]). In the present work the technique described in [6] is employed, with a quadratic interpolation scheme: the interpolation was performed using the point closest to the body surface (which can be either an internal or an external point) and the following point on the exterior of the cylinder. The interpolation is performed either in the streamwise or transverse direction, according to which one is closest to the local normal. An example of the nodes involved in the interpolation scheme is shown in Figure 1.2.

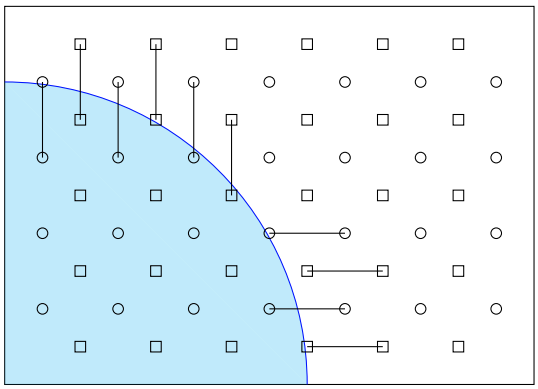

Figure 1.2: *Sketch of the points near the cylinder surface involved in the interpolation. The squares and the circles represent the points in which the horizontal and vertical velocity components (named u and v) have been interpolated, respectively.*

There are many benefits in the usage of an immersed boundary approach: the primary advantage of this method is associated with the fact that grid generation is greatly simplified. Generating body-conforming structured or unstructured grids is usually very difficult. Indeed, we want to build a grid that provides adequate resolution near the body with the minimum number of total grid points. These conflicting requirements can lead to a deterioration in grid quality, which can negatively impact the accuracy and the convergence properties of the solver. In addition, even for simple geometries, generating a good body-conforming grid can be an iterative process requiring significant efforts. As the geometry becomes more complicated, the task of generating an acceptable grid becomes increasingly difficult. The usage of the immersed-boundary method is also convenient

for flows with moving boundaries. The design of such complicated grids may require the generation of a new grid at each time step as well as a procedure to interpolate the solution at the previous time step to this new grid. Both of these steps can negatively impact the, accuracy, robustness, and computational cost of the solution procedure, especially in cases involving large motions. Thus, due to its inherent simplicity, the immersed boundary method represents an extremely attractive alternative for such flows.
One of the disadvantages of the method is related to the imposition of the boundary conditions, which is not straightforward. Moreover, the alignment between the grid lines and the body surface in body-conformal grids requires a good control of the grid resolution in the vicinity of the body and this has implications for the increase in grid size with increasing Reynolds number.

CHAPTER 2

Validation cases

A preliminary step, before performing the linear stability analysis around two cylinders in side-by-side arrangement, was the validation of all the codes used during this work. For this reason, the present chapter is devoted to a deep and complete check of all of the software tools needed for the simulations. The tests have been performed using a software package implemented in the CPL language by Prof. Flavio Giannetti.

Name	Description
BASE_FLOW_MB_vort	Computes a steady solution of the incompressible Navier-Stokes equations, using Newton iterations starting from a randomly perturbed flow field or from a previously computed solution.
BFGLOBALMODES_ARPACK_MB_vort	Computes direct and/or adjoint global modes associated with a given base flow using the implicitly restarted Arnoldi algorithm implemented in the ARPACK library with a shift-invert strategy.
CONTINUATION_vort	Allows one to perform base flow continuation and global-mode neutral curve tracking with respect to pre-defined parameters using the LOCA library of continuation algorithms.

Table 2.1: *Solvers used for computing the base flow, the eigenvalues/eigenvectors and to continue the solution. The denomination "vort" indicates the type of boundary condition used by the software.*

Name	Description
BFRF	Translates the binary flow data of the computed base flow in a format suitable for Newton restart.
PBF	Adds a pre-defined perturbation to the given base flow with given amplitude. The perturbation can be a random field or a Gaussian-shaped spot at a precise spatial location.
GMPBF	Adds the real part of an already computed direct global mode multiplied by a given amplitude to the related base flow.
BFIG	Produces an initial guess for the Newton solver starting from a base flow computed on a domain with a reduced streamwise extent. The missing data on the larger domain are replaced by a uniform flow whose modulus is equal to 1.

Table 2.2: *Pre-processing software used to modify a computed baseflow and to calculate the solution on an extended domain.*

Name	Description
BFPOST_MB_vort	Post-processing of a computed flow field stored in the "BaseFlow.bin" file located in the working directory.
BFSP	Computes the stagnation point in a small square region of a given flow field using Newton iterations.
BFGMPOST_ARPACK_MB_vort	Post-processing of the computed direct/adjoint global modes. For the sensitivity post-processing both modes are required.

Table 2.3: *Post-processing software containing all the data used to produce output.*

The programs can be divided into three categories: solvers, pre-processing tools and post-processing tools. The solvers represent the core of the package, performing the numerically solution of the steady and time-dependent incompressible Navier–Stokes equations and the computation of the required portion of the spectrum, specifying the shift on the imaginary axis and the number of eigenvalues to be computed. The direct and

adjoint eigenvectors can be computed as well. The output of the simulations is given in the form of binary files. The pre-processing codes are employed before starting the simulation since they provide all the preliminary data necessary to run the simulations (*i.e.* the files containing the initial conditions). Finally, the post processing tools provide raw data to be elaborated with *Matlab*® to produce all of the images. In Tables 1.1-1.3 the different codes are briefly described, divided by category.

2.1 Flow around a circular cylinder

The case studied for the validation of the codes is the flow around a single circular cylinder; the choice was made on the grounds that it is a well known flow, and since it has been extensively investigated both numerically and experimantally, many results are available in the literature, thus they can be assumed as a reference. The results reported in the literature have been used to validate the 2D base flow solver, the eigenfuction computation, the neutral-curve-tracking algorithm and the structural-sensitivity calculation. The geometry of the flow field is depicted in Figure 2.1. The reported dimensions are those referred to the M1 grid.
The reference system is placed in the centre of the cylinder. The boundary conditions employed in the code consist of a set of homogeneous Dirichlet conditions for what concerns the normal velocity components on the Γ_{up}, Γ_{down}, Γ_{in} boundaries, coupled with a constraint on the vorticity in order to simulate the flow far from the body; a condition on the reduced pressure and on the velocity derivative with respect to the x direction is set on the outlet boundary:

$$\Gamma_{up}: \begin{cases} v = 0 \\ \omega = 0 \end{cases} \quad \Gamma_{down}: \begin{cases} v = 0 \\ \omega = 0 \end{cases} \quad \Gamma_{in}: \begin{cases} u = U \\ \omega = 0 \end{cases} \quad \Gamma_{out}: -p + \frac{1}{Re}\frac{\partial u}{\partial x} = 0 \tag{2.1}$$

where u and v represent the velocity vector component in x and y direction respectively, ω is the flow vorticity and p is the reduced pressure.
Different meshes have been employed, to validate the results reproducing the same conditions presented in the reference articles, for the comparison to be fair, since some quantities are sensitive to a change of the domain size, as described in [7]. The characteristics of the exploited grids are reported in Table 2.4.
In order to better reconstruct the flow near the body and to resolve the details of the flow in the near wake, Roberts stretching transformations have been used to cluster the mesh points smoothly near the body. In particular, the coordinates (x_i, y_i) of a node in the computational mesh are obtained by evaluating the following expressions:

$$x_i = x_c \left\{ 1 + \frac{sinh[\tau_x(\frac{i}{n_x} - B_x]}{sinh(\tau_x B_x)} \right\}, \qquad y_i = y_c \left\{ 1 + \frac{sinh[\tau_y(\frac{i}{n_y} - B_y]}{sinh(\tau_y B_y)} \right\}, \tag{2.2}$$

where i and j are the grid indices and B_x and B_y are cofficients given by

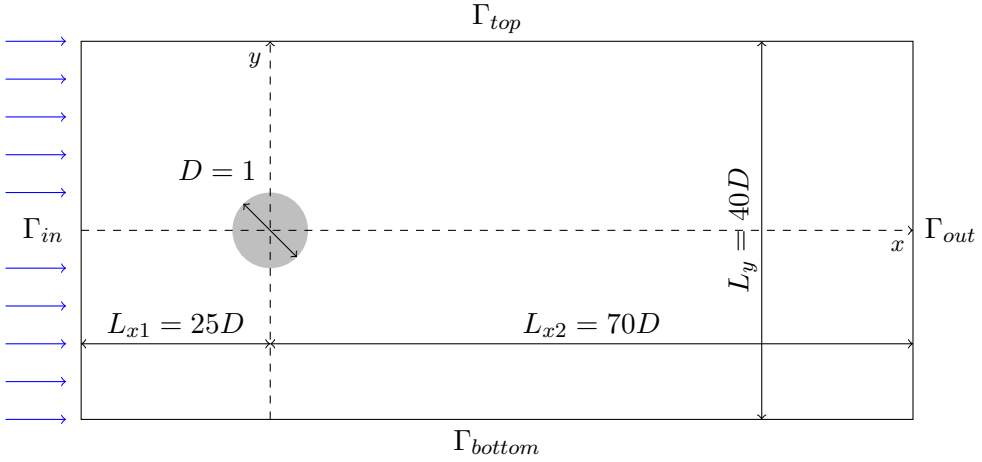

Figure 2.1: *Sketch of the computational domain using mesh M1.*

$$B_x = \frac{1}{2\tau_x} ln\left[\frac{1 + exp(\tau_x - 1)(x_c/L_x)}{1 + exp(-\tau_x - 1)(x_c/L_x}\right], \quad B_x = \frac{1}{2\tau_y} ln\left[\frac{1 + exp(\tau_y - 1)(y_c/L_y)}{1 + exp(-\tau_y - 1)(y_c/L_y}\right]. \tag{2.3}$$

In these formulae, L_x and L_y represent the number of points used in the directions, while n_x and n_y denote the number of points used in the x and y directions, respectively. τ_x and τ_y are two stretching parameters, which control the clustering of points and can range from zero (no stretching) to large values, in order to produce the largest refinement near the body.

Mesh	$x_{-\infty}$	$x_{+\infty}$	$y_{-\infty}$	$y_{+\infty}$	s_m	n_e	$n_{d.o.f}$
M1	-25	50	-20	20	0.013	$[600] \times [350]$	630000
M2	-25	140	-20	20	0.008	$[900] \times [420]$	1134000
M3	-60	200	-30	30	0.020	$[870] \times [450]$	1174500
M4	-45	125	-45	45	0.011	$[700] \times [550]$	1155000

Table 2.4: *Comparison between the different meshes used for the validation of the code: $x_{-\infty}$ and $x_{+\infty}$ are the locations of the inlet and outlet, respectively, while $y_{-\infty}$ and $y_{+\infty}$ are the positions of the upper and lower boundary; s_m accounts for the mesh stretching near the body and the lower is this value, the more dense is the mesh; finally, n_e and $n_{d.o.f}$ represent the number of points and the number of degrees of freedom (*i.e. *the size of the system matrix), respectively, in the whole domain.*

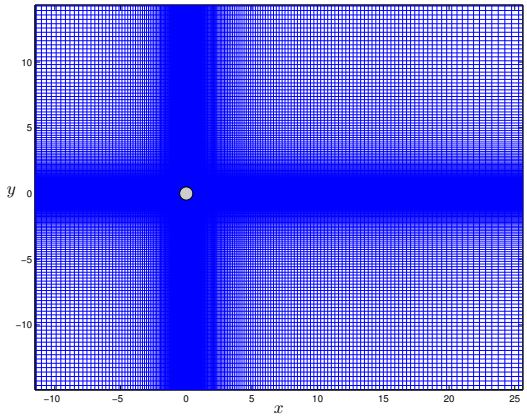

Figure 2.2: *Example of mesh (M1) used for the validation case. The number of points in x and y direction are $nx = 600$ and $nx = 350$ respectively.*

2.1.1 Base flow

To validate the solver of the base flow, different quantities have been evaluated; in particular, considering a range of Reynolds numbers for which the base flow presents a recirculation bubble downstream the cylinder, as shown in Figure 2.3, the drag coefficient C_D and the length of the wake bubble L_w, adimensionalized with respect to the cylinder diameter D have been measured. The data have been compared with several numerical experiments carried out by many other authors, see Tables 2.5 and 2.6.

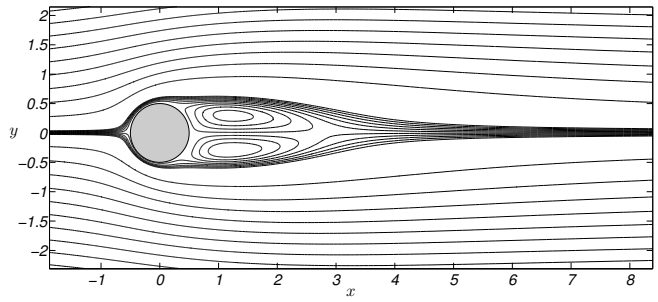

Figure 2.3: *Streamlines of the flow around a circular cylinder at $Re = 40$. The presence of the recirculation bubble behind the cylinder is evident.*

Good agreement has been found with the values obtained in the majority of the cited works. However, for what concerns some data, there are significant differences: for instance, looking at the recirculation bubble length (Table 2.5), Coutanceau & Bouard (1977) obtained a set of results which do not match perfectly with those computed using

	$Re = 20$	$Re = 40$
Dennis & Chang (1970)	0.94	2.35
Coutanceau & Bouard (1977)	0.73	1.89
Fornberg (1980)	0.91	2.24
Ye *et al* (1999)	0.92	2.27
Giannetti & Luchini	0.92	2.24
Lima E Silva *et al* (2003)	1.05	2.55
Current (M1)	0.90	2.24
Current (M2)	0.89	2.22

Table 2.5: *Comparison of the bubble length computed by several authors for two different Reynolds numbers. M1 and M2 indicate the type of mesh used for the validation.*

	$Re = 10$	$Re = 20$	$Re = 40$	$Re = 50$
Dennis & Chang (1970)	...	2.05	1.52	...
Fornberg (1980)	...	2.00	1.50	...
Ye *et al* (1999)	...	2.03	1.52	...
Giannetti & Luchini (2007)	...	2.05	1.54	...
Lima E Silva *et al* (2003)	2.80	2.05	1.55	1.50
Current (M1)	2.79	2.02	1.51	1.38
Current (M2)	2.79	2.02	1.51	1.38

Table 2.6: *Comparison between the C_D for different Reynolds numbers. The symbols M1 and M2 indicate the type of mesh used for the validation.*

meshes M1 and M2, with a deviation from our results of 35%; the difference with data reported by Lima E Silva *et al* (2003) is order of 31% with respect to the results acquired with the two meshes considered. For what concerns the C_D coefficient, a slight deviation can be observed for $Re = 50$. Lima E Silva *et al* (2003) obtained a $C_D = 1.495$ which is 11.5% higher than the present one. This is probably due to the fact that, in their work, Lima E Silva *et al* used a uniform grid instead of a stretched one, as in the case of M1 and M2, and this could lead to slightly different values if the grid is too coarse in the proximity of the body.
As a whole, the data extracted from the validation runs seem to match very well the results obtained by other authors, showing that the code is reliable and robust: in fact, the two meshes M1 and M2 were chosen to test the sensitivity of C_D and $\frac{L_w}{D}$ with respect to mesh refinement and domain size. In this sense, the tests carried out using different domains and meshes highlight that the calculations can be considered converged up to three significant digits.

2.1.2 Eigenvalues and eigenvectors

To validate the computation of the eigenvalues, the results reported by Sipp & Lebedev (2007) were taken as reference: in their work, they computed a wide portion of the spectrum of the base flow for a circular cylinder at $Re = 46.6$; this value is critical because a Hopf bifurcation occurs, *i.e.* a couple of complex-conjugate eigenvalues cross the imaginary axis leading to an instability in the flow. In particular, Figure 2.4 shows that a marginally stable eigenvalue at $\omega = 0.74$ is crossing the imaginary axis.
The validation was performed by comparing only the marginally stable eigenvalue, because the three branches depicted in the figure are ill-conditioned, thus they depend on the mesh resolution and on the method used to discretize the problem. This fact does not invalidate our results since the system dynamics for long times is led by the least stable eigenvalue, which can be accurately computed. The comparison with the reference results is reported in Figure 2.4, where the computed eigenvalue is marked with a red diamond near the imaginary axis, and in Figures 2.5 and 2.6. As can be seen, the comparison is very good, with an error of 0.89% for the imaginary part. The computation was made with the mesh M3 which has the same dimensions of the one used in the paper by Sipp & Lebedev (2007). For sake of completeness, the corresponding direct and adjoint modes have been reported and, as one may note, they match very well with the ones reported in [12]. The different values in the colorbars are due to a different scaling used for the eigenvectors.

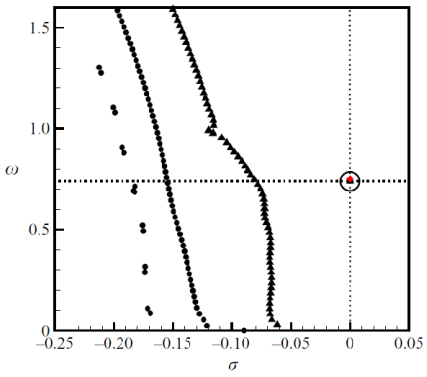

Figure 2.4: *Comparison between the two spectrum portions of the baseflow of a circular cylinder at* $Re = 46.6$. *The dashed lines indicate the position of the reference least stable eigenvalue, denoted by a black triangle in the complex plane, while the red rhombus represents the eigenvalue computed with mesh M3. The corresponding complex-conjugate eigenvalue it is not reported here.*

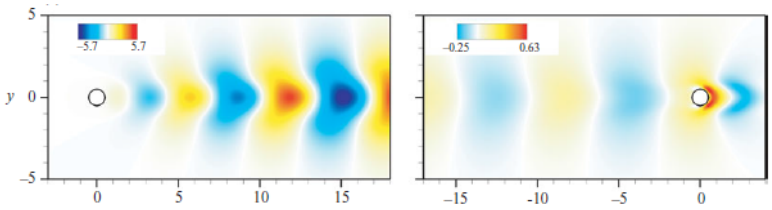

Figure 2.5: *Direct and adjoint modes computed by Sipp & Lebedev (2007) [12] at* $Re = 46.6$ *corresponding to the marginally stable eigenvalue depicted above.*

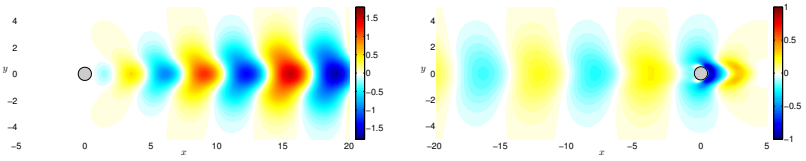

(a) *Direct mode .* **(b)** *Adjoint mode.*

Figure 2.6: *Direct and adjoint modes computed using the mesh M3 at* $Re = 46.6$ *corresponding to the marginally stable eigenvalue depicted above.*

2.1.3 Structural sensitivity

To test the computation of the structural sensitivity, a comparison with the work performed by Giannetti & Luchini (2007) was attempted. In this case the structural sensitivity for $Re = 50$ was computed using the mesh M1. The result shows that the reference and computed sensitivity parameters match almost perfectly: in fact the same isolines are employed in Figure 2.7 and 2.8 and looking at the colorbar, even the peak behind the cylinder is very close to the one obtained by Giannetti & Luchini. The little differences between the two results may be attributed to the different boundary contions used in the simulation and a different kind of discretization near and behind the cylinder.

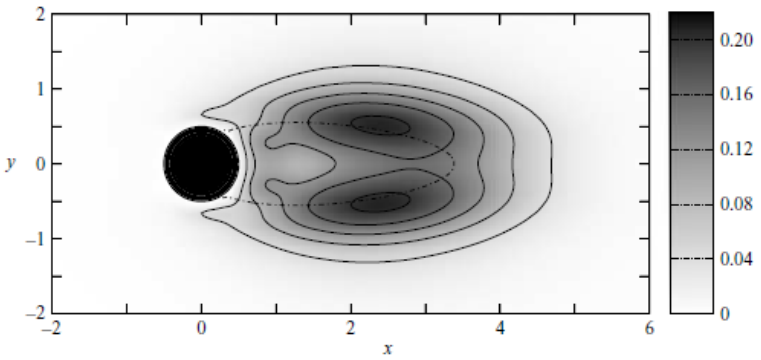

Figure 2.7: *Structural sensitivity parameter for the flow past a circular cylinder for* $Re = 50$*, Giannetti & Luchini (2007). Only the relevant area of the domain is shown.*

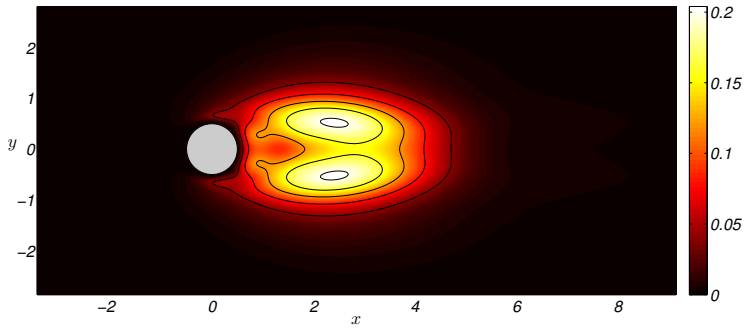

Figure 2.8: *Structural sensitivity parameter for the flow past a circular cylinder for* $Re = 50$ *computed using the mesh M1. Only the relevant area of the domain is shown.*

2.1.4 Neutral curves

To validate the neutral-curve-tracking algorithm, the results reported in [8] were taken as a reference. Figure 2.9 shows the neutral curves for the bi-dimensional flow past a rotating cylinder varying the two governing parameters, *i.e.* the Reynolds number and the adimensional angular velocity, defined as

$$Re = \frac{UD}{\nu} \qquad \text{and} \qquad \alpha = \frac{\Omega D}{2U}, \tag{2.4}$$

where U represents the free-stream velocity, D is the cylinder diameter, ν denotes the kinematic viscosity and Ω represents the angular velocity of the cylinder.
Two critical modes are present, and the neutral curve associated with Mode I was considered for the validation. When the cylinder is still ($\alpha = 0$) the the critical Reynolds number is $Re = 46.6$ and the frequency of the marginally stable mode is $Im(\sigma) \approx 0.74$, which confirms the results reported in the previous paragraph. When the body starts rotating, the frequency of the least stable mode increases and the critical value of α reaches an almost costant value $\alpha \approx 1.9$.
The computation was performed using the mesh M4. The blue circles reported in Figure 2.9 represent the computed neutral curve. As one may note, the neutral curve computed in this work matches almost perfectly the reference one, confirming the accuracy of the employed code.

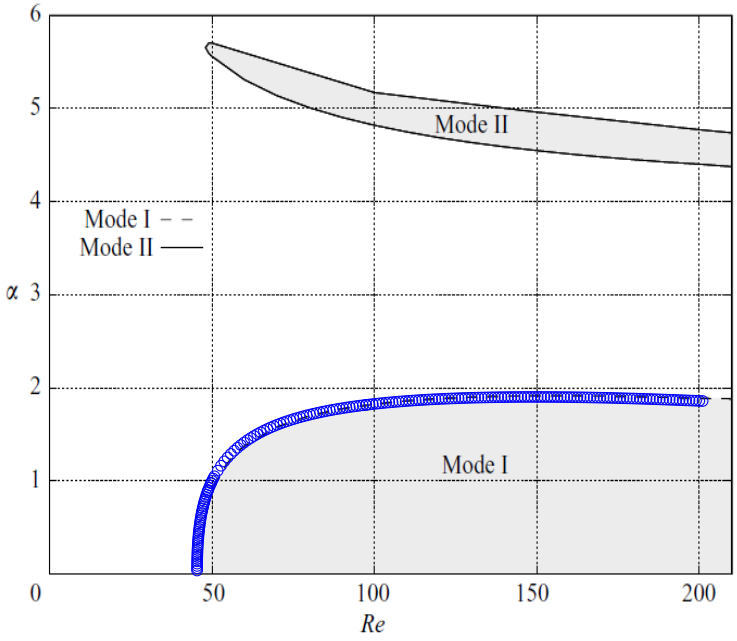

Figure 2.9: *Neutral curve of the Mode I for a rotating cylinder in the parameter plane the Reynolds number Re–adimensional angular velocity α. The circles correspond to the present results computed with mesh M4.*

CHAPTER 3

Results

This chapter is concerned with the results of the global stability analysis for two cylinders in side-by-side arrangement. This kind of analysis has been performed by several authors ([5], [7], [9]) but in all of the previous studies the considered base flow was symmetric. The only work in which the asymmetric base flow was analysed, is the Ph. D. thesis by M. Carini [10]. In his work, the author performed an extensive analysis, drawing all the neutral curves which delimit the stability and instability areas for both the symmetric and asymmetric base flows, in the parameter space. His results, which are reported in Figure 0.2 of the Introduction, are the starting point of this analysis. In fact, some of the eigenvalues related to the neutral curves, which delimit the region in the parameter space where the asymmetric base flow is stable, show a dependency on the domain length. In particular, the one associated with the red continuous neutral curve, which marks the upper boundary of the blue region. For this reason, the objectives of the present work are two:

- to establish the minimum length of the computational domain for which the neutral curves, that delimit the asymptotic stability area of the asymmetric base flow, can be considered converged. Convergence has been checked with respect to the least stable eigenvalue computed in the neighbourhood of the neutral curve. The calculation has been considered converged, and the domain sufficiently long, if the least stable eigenvalues computed on the grid and on longer grids agreed up to four significant digits.
- to delimit the stability region of the asymmetric base flow by a sufficiently long grid.

The chapter begins with a description of the problem geometry and boundary conditions used for the simulations. In Section 3.2 the asymmetric base flow is described. In Section 3.3 the sensitiviy of the eigenvalues to the domain length is investigated, completed by

an analysis of the structural sensitivity of the far-wake mode 5. In section 3.4 the neutral curves are traced using a suitable domain length and the new stability area is illustrated in Section 3.5. Finally, Section 3.6 is devoted to a comparison between the linear stability results and DNS simulations.

3.1 Initial geometry of the problem

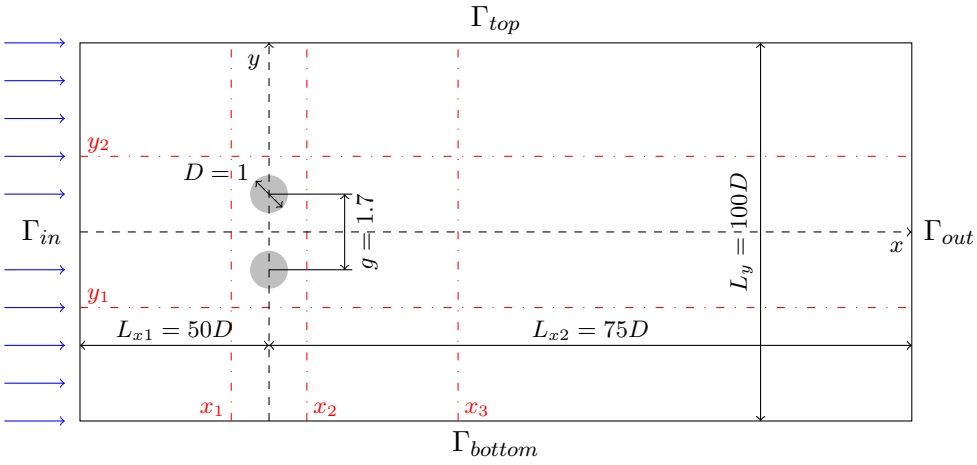

$$Re = \frac{UD}{\nu} \qquad g = \frac{L}{D}$$

Figure 3.1: *Sketch of the initial computational domain; the parameters which govern the flow pattern are reported in the box.*

The initial domain used for the simulations has a length $L_x = 125D$ (where D is the cylinder diameter) and the two cylinders are placed at a distance $50D$ from the inlet boundary. For convenience, all the reported lenght are nondimensionalised by the diameter. The reference system is placed with the x axis coincident with the symmetry axis and the y axis passing through the cylinder centres. The mesh has been splitted in four parts in the horizontal direction and in three parts in the vertical direction. Every part has a different number of points in order to refine the mesh near the two bodies and to better resolve the flow pattern behind the cylinders. The red lines in Figure 3.1 represent the boundary of the different regions in which the domain has been divided to build the mesh. All the data relative to the geometry and the grid are reported in Table 3.1 and 3.2.
It is easy to note that the grid is thickened near the bodies, in both directions: in fact the grid is denser in the interval $[x1, x2]$ and $[y1, y2]$.
The boundary conditions are the same used in the validation case:

Domain size	L_x	L_y	$x_{-\infty}$	$x_{+\infty}$	$y_{-\infty}$	$y_{+\infty}$
	125	100	-50	75	-50	50
Region size	$[0, x_1]$	$[x_1, x_2]$	$[x_2, x_3]$	$[0, y_1]$	$[y_1, y_2]$	
	$[0, 49]$	$[49, 51]$	$[51, 61]$	$[0, 47.5]$	$[47.5, 52.5]$	

Table 3.1: *Geometric parameters adopted: L_x and L_y are the dimensions of the domain while $x_{-\infty}$, $x_{+\infty}$, $y_{-\infty}$ and $y_{+\infty}$ are the coordinates of the inner, outer, upper and lower boundaries according to the reference system represented in Figure 3.1. In the inner data row, the coordinates of the different intervals are reported. The last part of the domain in the x and y directions, i.e. $[x3, end]$ an $[y2, end]$, has been omitted.*

n_e	n_{dof}	nx_1	nx_2	nx_3	nx_4	ny_1	ny_2	ny_3
$[430] \times [450]$	139500	100	100	100	130	100	250	100

Table 3.2: *Resolution adopted for the shortest domain: n_e indicates the number of grid points, n_{dof} represents the number of degrees of freedom in the computational domain and nx_i and ny_j are the number of points in the x and y directions, respectively, used in every region.*

$$\Gamma_{up} : \begin{cases} v = 0 \\ \omega = 0 \end{cases} \quad \Gamma_{down} : \begin{cases} v = 0 \\ \omega = 0 \end{cases} \quad \Gamma_{in} : \begin{cases} u = U \\ \omega = 0 \end{cases} \quad \Gamma_{out} : -p + \frac{2}{Re}\frac{\partial u}{\partial x} = 0. \tag{3.1}$$

As one may note, the vorticity far from the body is set to zero to reduce the confinement effects. Consequently, the flow on Γ_{in}, Γ_{up} and Γ_{down} can be considered as a potential flow.

3.2 Asymmetric base flow

The asymmetric base flow was initially computed at $Re = 68$ and $g = 1.7$ in the computational domain described above. The computation of the asymmetric solution started using the symmetric base flow and perturbing it with the real part of the eigenvector associated to $\mu = 0$, being μ the imaginary part of the eigenvalue. The perturbed solution was then used as initial guess for the Newton iteration, which converged to the asymmetric steady solution. The streamlines of the asymmetric baseflow and the modulus of the velocity are reported in Figure 3.2 and 3.3. The considered baseflow is characterised by two recirculation bubbles of different sizes. Actually, there are two, equivalent, base flows, each one obtained from the other by a reflection around the symmetry axis. The two base flows have the same stability properties. They can both be obtained from the Newton iteration, depending on the initial guess. In the present calculation the smaller

recirculation bubble is located behind the upper cylinder while the larger one is located behind the lower cylinder. The presence of these recirculation bubbles is confirmed by Figure 3.3: in fact, two low-speed regions, coloured in blue can be observed behind the cylinders. In these areas the absolute value of the velocity is nearly zero testifying the presence of two separation regions behind the cylinders. The speed through the gap between the two bodies is 20% higher than the free stream velocity because of the presence of the bodies.

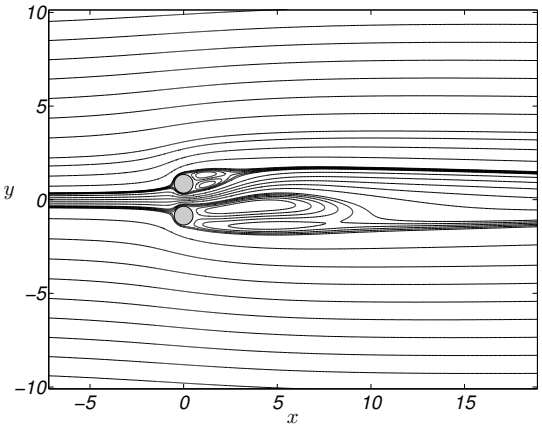

Figure 3.2: *Streamlines of the asymmetric base flow around two cylinders in side-by-side, arrangement,* $Re = 68$ *and* $g = 1.7$.

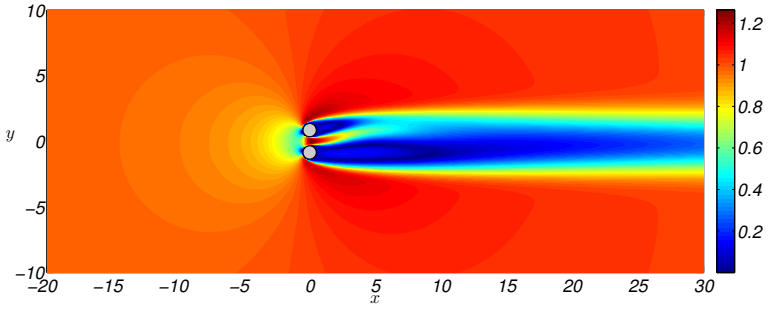

Figure 3.3: *Modulus of the velocity of the asymmetric base flow around two cylinders in side-by-side arrangement,* $Re = 68$ *and* $g = 1.7$.

3.3 Eigenvalue computation

The computation of the eigenvalues was performed using different domain lengths in the point $g = 1.7$ and $Re = 68$ to investigate the behaviour of the mode related to

the neutral curve associated with the far-wake mode 5 with respect to an increase of the domain length, to obtain a reliable, *i.e.* converged, neutral curve. In particular, the presence of a cusp near this point raises doubts about the accuracy of the curve. Starting from a length $L_x = 125$, the domain has been stretched by steps of 25 diameters up to $L_x = 400$. Then, steps of 50 diameters were used to further increase the domain length up to the maximum extension $L_x = 950$.

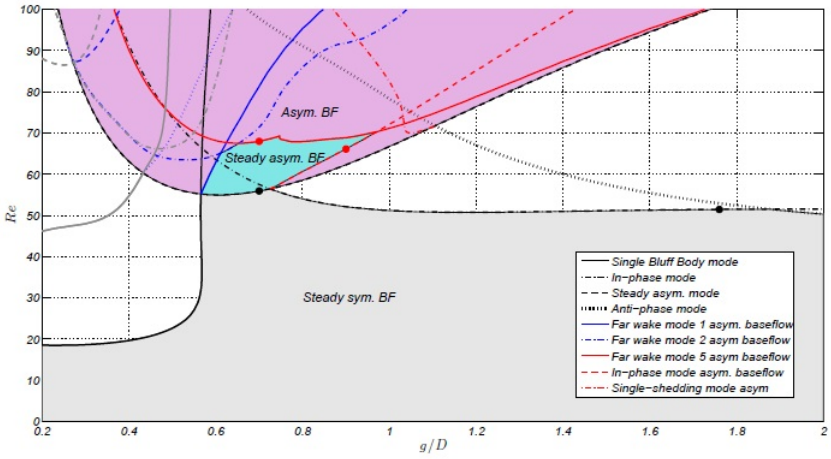

Figure 3.4: *Neutral curves in $g - Re$ plane, for a domain length $L_x = 125$ as computed by M. Carini in [10].*

Figure 3.5 reports the result of the eigenvalue computation for different extensions: for clarity, only few domains have been reported. In fact, as one may note, several eigenvalues have been computed and plotting the results for all the domains considered would have made the graph completely unintelligible.
The following shifts s_i were considered in the eigenvalue computation, in order to scan the spectrum near the imaginary axis and to compute any potential marginally stable eigenvalue:

$$s_1 = 0.0 + 0.1i, \quad s_2 = 0.0 + 0.35i, \quad s_3 = 0.0 + 0.6i, \quad s_4 = 0.0 + 0.85i. \tag{3.2}$$

For the shortest domain, there is an unstable eigenvalue located at $\mu \approx 0.395$ (the eigenvalue corresponding to the far wake mode 5 in Figure 3.4). The analysis with extended lengths reveals that the unstable eigenvalue is isolated from a branch which has been reconstructed only for the longest domain.
Even though the initially unstable eigenvalue remains isolated from the branch, its identification is not trivial; in fact, when the domain length is increased, both its real and imaginary part change. For instance, considering the length $L_x = 125$, this eigenvalue is $\lambda \approx 1 \cdot 10^{-3} + 0.394i$ while using the longest domain it becomes $\lambda \approx -4.4 \cdot 10^{-3} + 0.402i$. Figures 3.7(a), 3.7(b), 3.8(a) and 3.8(b) report the real and imaginary part of the eigenvalue, as a function of the domain length. It can be noted that the imaginary part can

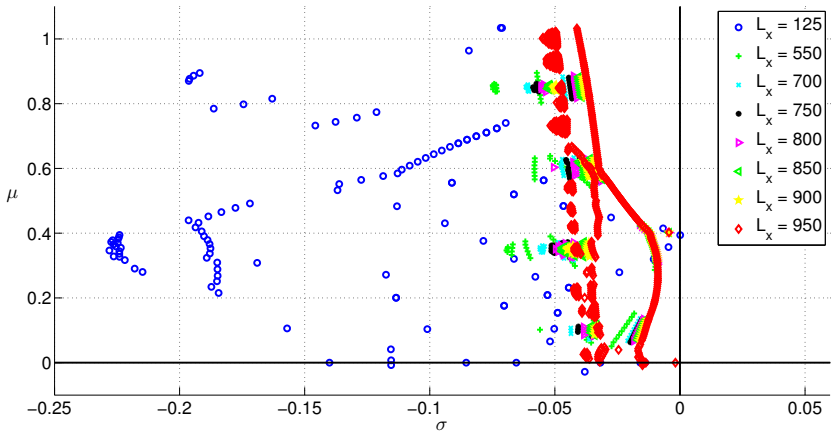

Figure 3.5: *Portion of the spectrum at $Re = 68$ and $g = 1.7$ for different domain sizes. The entire branch has been reconstructed for the longest domain ($L_x = 950$).*

be considered converged up to four digits only for domains with $L_x \geq 550$. Interestingly, the real part of the eigenvalue depends quite strangely on the domain length, because it tends to oscillate around the value of $\sigma = -4.4 \cdot 10^{-3}$, making its evaluation non-trivial.

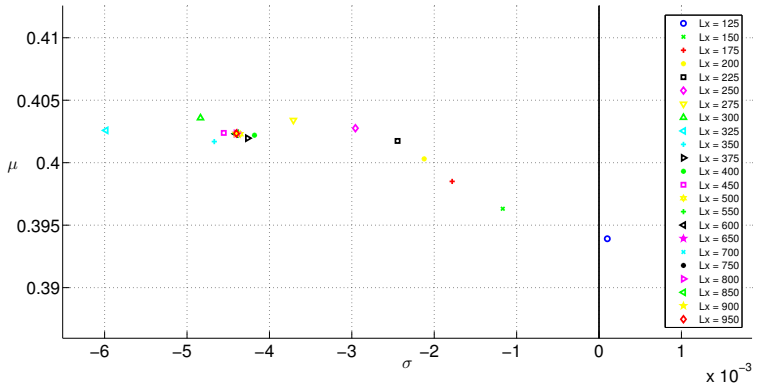

Figure 3.6: *Position in the complex plane of the initially unstable eigenvalue (blue dot) for different domain lengths.*

This results are useful to evaluate which is the most appropriate domain length that has to be used to reconstruct the whole stability area. Unfortunately, different branches of the neutral curve require different domain sizes. For instance, let us consider the far wake mode 5, which delimits the upper boundary of the stability area: since the real and imaginary parts of the corresponding eigenvalue are converged to the fourth decimal digit for $L_x = 550$, this length has been identified as the most appropriate one to compute

the neutral curve. A different result has been obtained considering the neutral curve associated with the Far wake mode 1. In fact, in this case, the length $L_x = 550$ is not adequate, since the eigenvalue associated with the corresponding mode has not reached convergence yet. For this reason, the longest domain has to be used in this case. Figures 3.7(c), 3.7(d), 3.8(c) and 3.8(d) confirm this result, showing the trend of the real and imaginary part of the eigenvalue related to the far wake mode 1, as a function of the domain size, for the parameters g =1.59 and Re = 70. Further results and a more detailed analysis concerning all the neutral curves delimiting the stability area are presented in the next section.

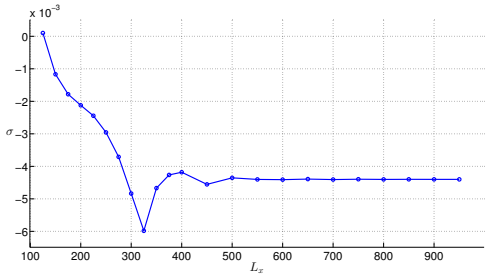

(a) $\sigma = \sigma(L_x), Re = 68, g = 0.7$.

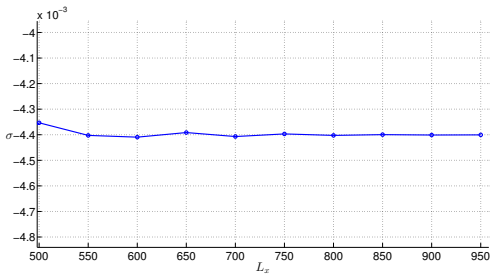

(b) *Zoom of the function* $\sigma = \sigma(L_x), Re = 68, g = 0.7$.

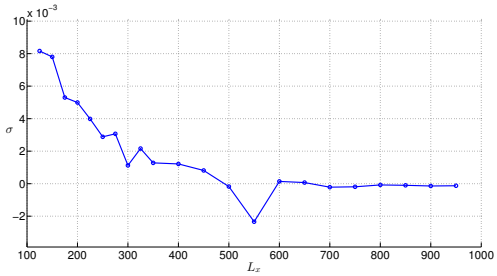

(c) $\sigma = \sigma(L_x), Re = 70, g = 0.59$.

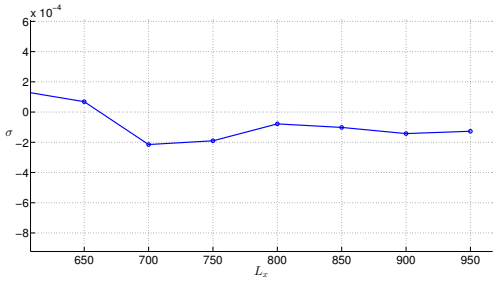

(d) *Zoom of the function* $\sigma = \sigma(L_x), Re = 70, g = 0.59$.

Figure 3.7: *Trend of the real part of two different marginally stable eigenvalues with respect to the domain length: in subfigures (a) and (b) the eigenvalue related to the far wake mode 5 is reported. Subfigures (c) and (d) show the trend of the eigenvalue corresponding to the far wake mode 1.*

In order to complete the analysis, the structural sensitivity of the unstable mode for $L_x = 550$ has been reported in Figure 3.10: as can be noticed, the core of the instability is located behind the lower cylinder confirming the results reported by Carini, Giannetti & Auteri in [10], making this area very sensitive to flow perturbations.

Figures 3.11, 3.12 and 3.13 report the direct and adjoint mode and the structural sensitivity associated with the, initially unstable eigenvalue, for different domain extensions

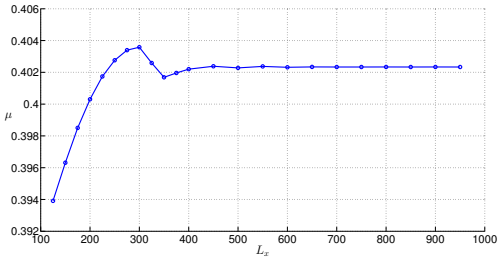

(a) $\mu = \mu(L_x), Re = 68, g = 0.7$.

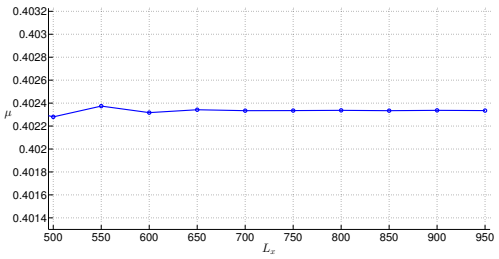

(b) *Zoom of the function* $\mu = \mu(L_x), Re = 68, g = 0.7$.

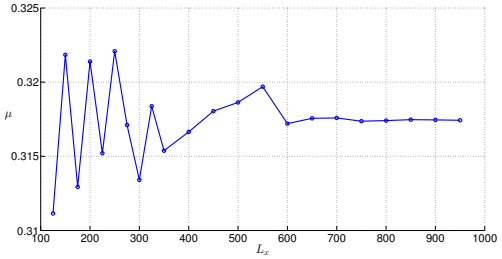

(c) $\mu = \mu(L_x), Re = 70, g = 0.59$.

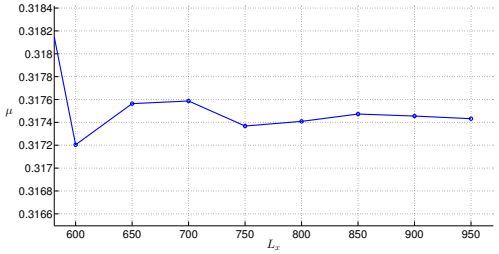

(d) *Zoom of the function* $\mu = \mu(L_x), Re = 70, g = 0.59$.

Figure 3.8: *Trend of the imaginary part of two different marginally stable eigenvalues with respect to the domain length: in subfigures (a) and (b) the eigenvalue related to the far wake mode 5 is reported. Subfigures (c) and (d) show the trend of the eigenvalue corresponding to the far wake mode 1.*

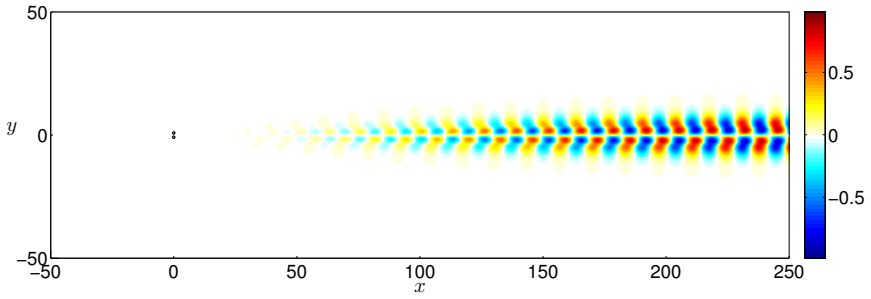

Figure 3.9: *Direct mode corresponding to the unstable eigenvalue at* $Re = 68$ *and* $g = 1.7$ *for* $L_x = 550$. *Only a part of the domain has been reported, because of its large extension.*

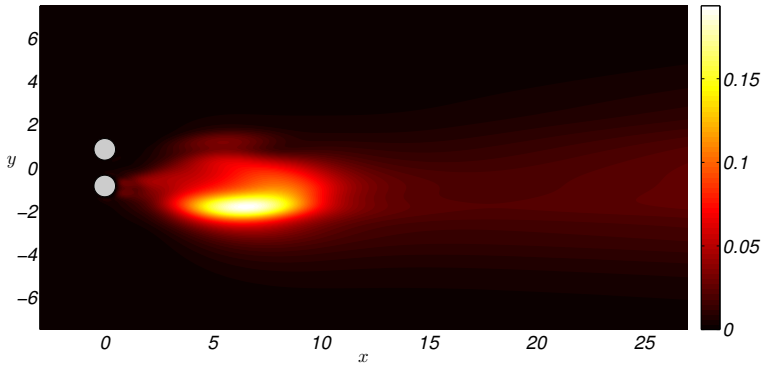

Figure 3.10: *Stuctural sensitivity of the unstable eigenvalue at* $Re = 68$ *and* $g = 1.7$ *for* $L_x = 550$*. Only the relevant portion of the domain is shown.*

($L_x = 125$, $L_x = 550$, $L_x = 950$) respectively. These lengths have been chosen for the comparison because they have been employed to reconstruct the neutral curves which delimit the stability area, therefore they are the most representative ones in the present study.
For the first two lengths, the mode is not completely contained in the domain, since the oscillations reach the outlet boundary. Only for the longest domain, the mode is able to fully develop, reaching its maximum in the region between $L_x = 300$ and $L_x = 400$, and then slowly decays. Comparing Figures 3.11(b) and 3.11(c) with Figure 3.9 little changes can be observed in the mode shape, changes which are due to the frequency drift.
The structural sensitivity for the two lengthened domains, sketched in Figure 3.12, exhibits a behaviour which is quite different to the one shown for the initial domain: in fact, the core of the instability is not captured on the shortest domain, confirming that the domain size must be sufficient to contain the region where the structural sensitivity is high to provide reliable results about the stability of the flow [7]. For this reason, the domain extensions from $L_x = 550$ to $L_x = 950$ show a good convergence of the least stable eigenvalue. In addition, the structural sensitivity parameter in Figure 3.12(a) appears to be less intense with respect to that reported in Figures 3.12(b) and 3.12(c), especially in the immediate neighbourhood of the two cylinders.
The adjoint mode related to the shortest domain, as depicted in Figure 3.13(a), shows a wavy pattern, with four peaks attached to the cylinders (they are not visible because of the large scale used). The intensitiy of these peaks increases as the domain length is increased.

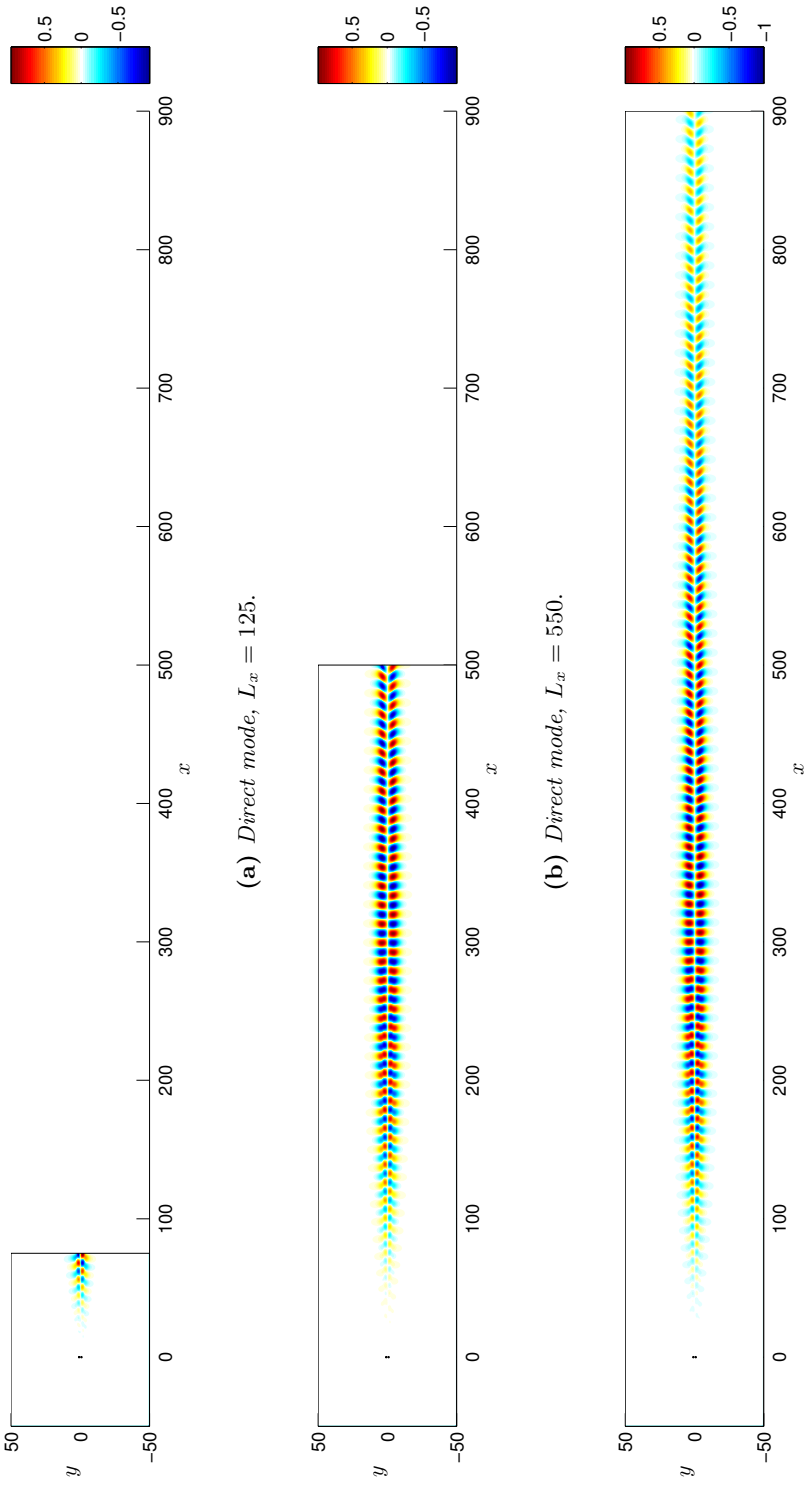

(a) *Direct mode,* $L_x = 125$.

(b) *Direct mode,* $L_x = 550$.

(c) *Direct mode,* $L_x = 950$.

Figure 3.11: *Direct mode related to the far wake mode 5 at* $Re = 68$ *and* $g = 1.7$ *for different domain lengths:* $L_x = 125$ *(**a**),* $L_x = 550$ *(**b**),* $L_x = 950$ *(**c**).*

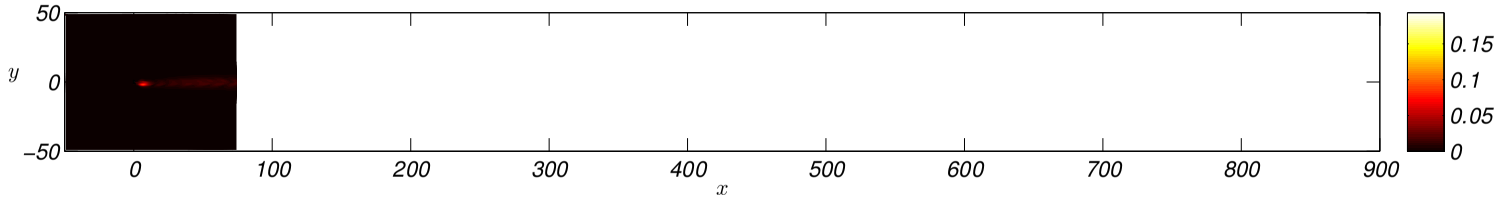

(a) *Structural sensitivity parameter,* $L_x = 125$.

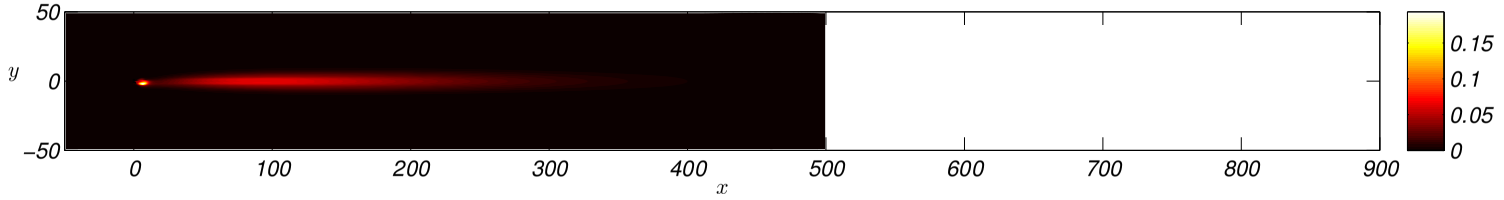

(b) *Structural sensitivity parameter,* $L_x = 550$.

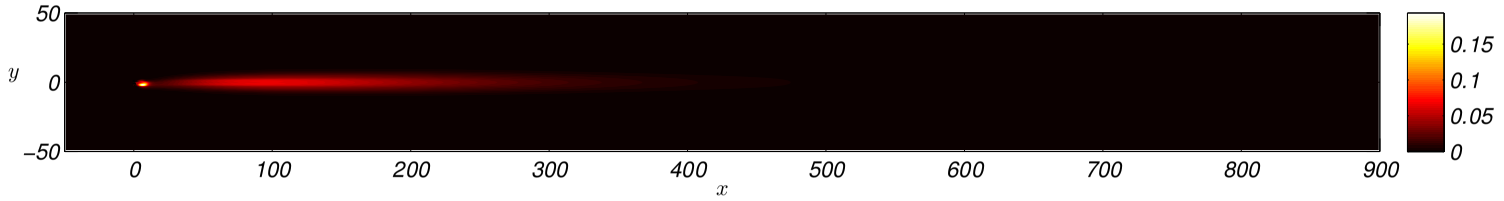

(c) *Structural sensitivity parameter,* $L_x = 950$.

Figure 3.12: *Structural sensitivity parameter related to the far wake mode 5 at* $Re = 68$ *and* $g = 1.7$ *for different domain lengths:* $L_x = 125$ ***(a)***, $L_x = 550$ ***(b)***, $L_x = 950$ ***(c)***.

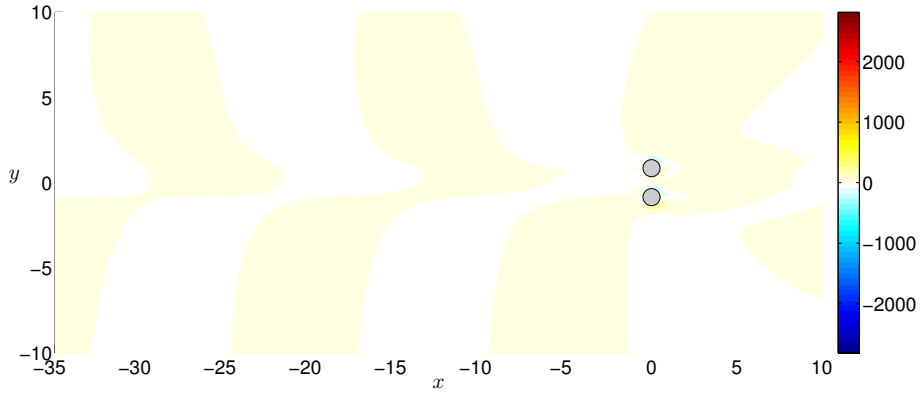

(a) *Adjoint mode,* $L_x = 125$.

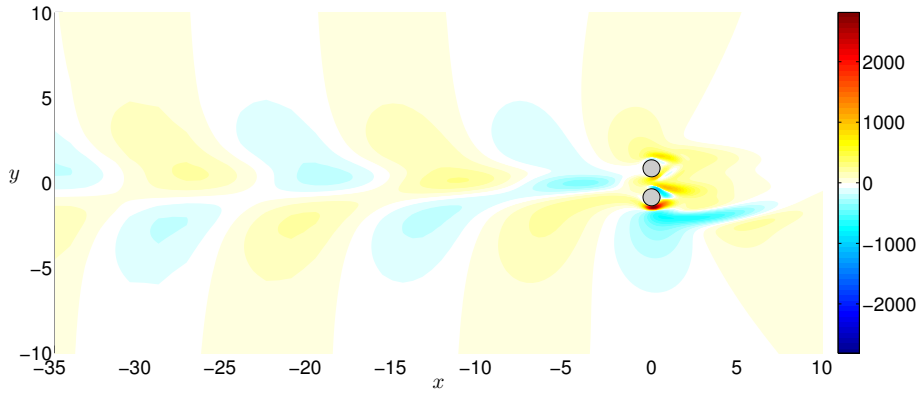

(b) *Adjoint mode,* $L_x = 550$.

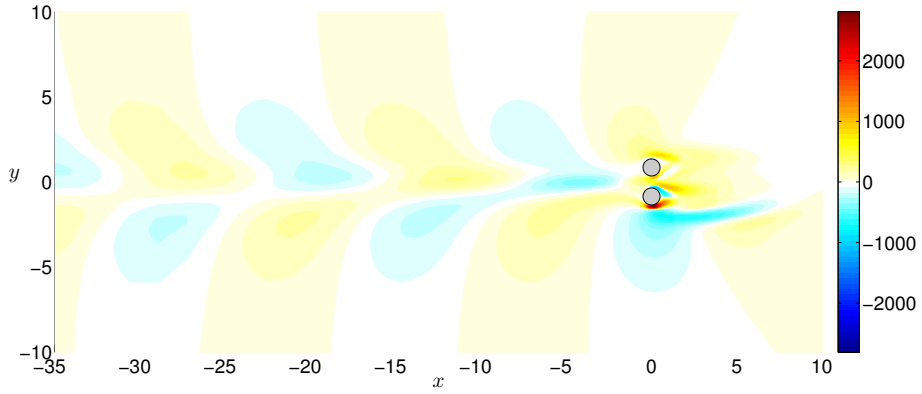

(c) *Adjoint mode,* $L_x = 950$.

Figure 3.13: *Adjoint mode corresponding to the far wake mode 5 at* $Re = 68$ *and* $g = 1.7$ *for different domain lengths:* $L_x = 125$ ***(a)***, $L_x = 550$ ***(b)***, $L_x = 950$ ***(c)***.

3.4 Neutral-curve tracking

In this section the neutral curves which delimit the stability area of the asymmetric base flow, calculated using the lengthened domains, are presented. The neutral curves plotted in colour are related to the asymmetric base flow, while that plotted in black belong to the symmetric base flow. Both flows have been considered, in fact the lower boundary of the stability area is related to a pitchfork bifurcation on the symmetric base flow. The impact of an increased domain length on these curves has been ascertained as well as it will be shown in the next paragraphs. Every section is dedicated to the description of a single neutral curve, integrated with a comparison with the corresponding one calculated by Carini and depicted in grey. Furthermore, for each neutral curve, the corresponding direct and adjoint modes and the structural sensitivity are reported in two points along the curve. In the final section the parameter space with all neutral curves is depicted, to illustrate how the asymptotic stability area is changed.

3.4.1 Far wake mode 5

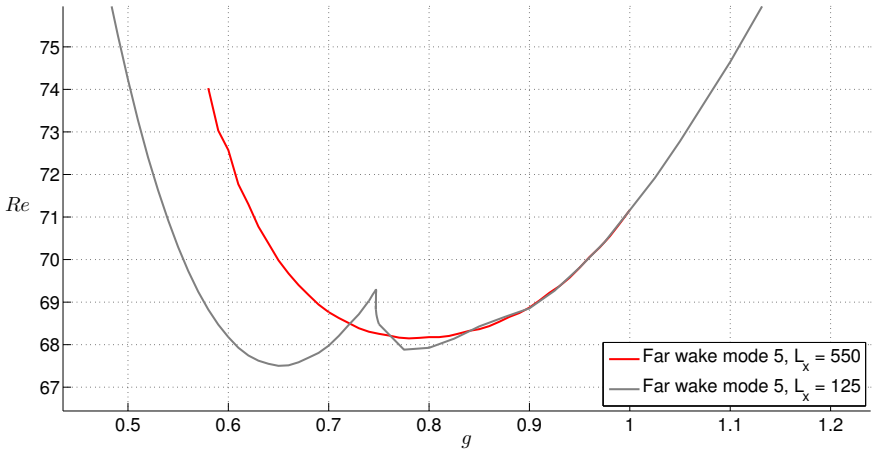

Figure 3.14: *Comparison between the neutral curves associated with the Far wake mode 5 computed using two different domain lengths:* $L_x = 550$ *(red curve) and* $L_x = 125$ *(grey curve).*

The neutral curve far wake mode 5 delimits the upper boundary of the stability region for the asymmetric base flow. It is associated with a marginally stable eigenvalue whose imaginary part is in the range $0.344 < \mu < 0.552$ and it is an almost linear function of the adimensional gap spacing, as reported in Figure 3.17. This curve has been obtained using a domain length of $L_x = 550$, since for this size of the domain the relative eigenvalue can be considered converged.
The comparison between this curve and that calculated with a domain length of $L_x = 125$, shows that its shape is markedly changed for $g < 0.9$: in fact, the peak in the point

$g \approx 0.75$, $Re \approx 69.1$ is present no more, making the upper boundary of the stability area smooth. In addition, the left part of the curve has the same slope of the old one, but it is placed on a higher set of Reynolds numbers, extending toward higher Reynolds numbers the upper boundary of the stability area.

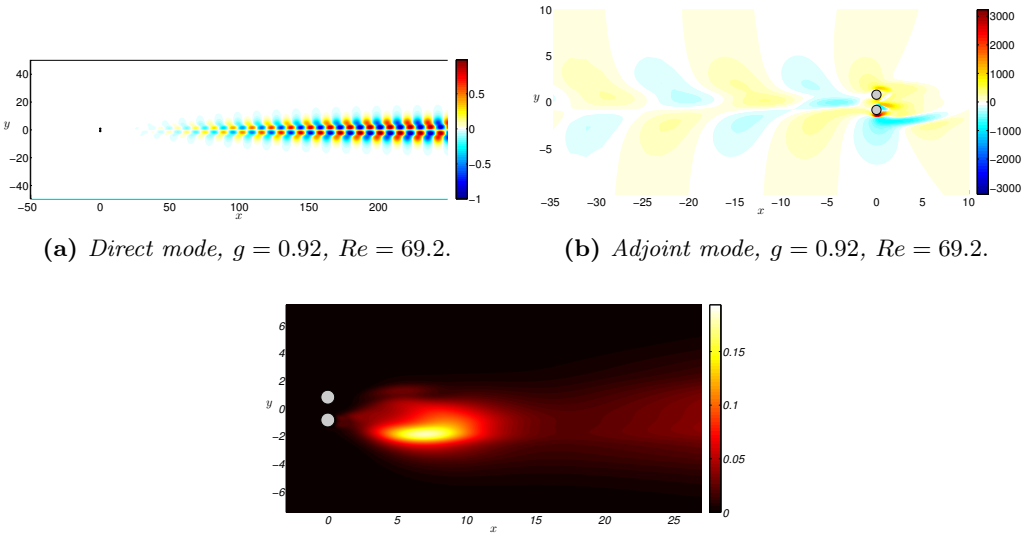

(a) *Direct mode,* $g = 0.92$, $Re = 69.2$.

(b) *Adjoint mode,* $g = 0.92$, $Re = 69.2$.

(c) *Structural sensitivity,* $g = 0.92$, $Re = 69.2$.

Figure 3.15: *Direct mode*(a)*, adjoint mode* (b) *and structural sensitivity* (c) *related to the far wake mode 5 in the point* $g = 0.92$, $Re = 69.2$.

3.4.2 In-phase asymmetric mode

The neutral curve associated with the in-phase asymmetric mode covers the right boundary of the above-mentioned area. The marginally stable eigenvalue which is connected to this neutral curve has an imaginary part which goes from $\mu \approx 0.627$ to $\mu \approx 0.689$, when the gap is increased from $g \approx 0.51$ to $g \approx 1.2$. The phase of this eigenvalue shows an oscillating trend until $g \approx 0.83$, then it increases. This curve does not change its position and shape when a longer domain, $L_x = 550$ in this case, is employed, as depicted in Figure 3.18. Is worth pointing out the fact that, starting from the point at minimum Reynolds number, $Re \approx 57$, only the right part of the curve exists. In fact, the left branch, is overlapped to the black neutral curve, associated with the in-phase mode present in the symmetric base flow; this is because the continuation algorithm jumps on a different branch when they cross, as described in [10].

3.4.3 Asymmetric mode

This curve, as one may note, has been plotted in black. As already said in the first part of this section, this means that the curve belongs to the symmetric baseflow. It delimits

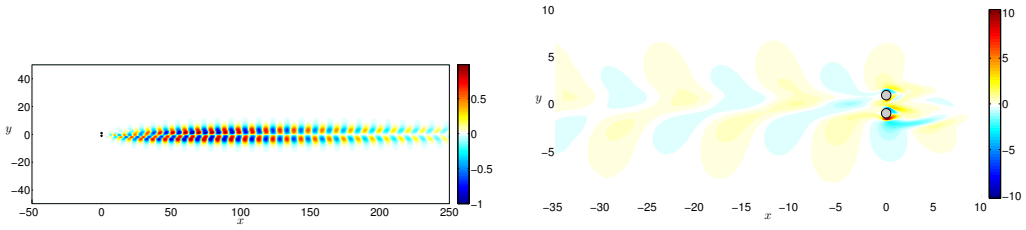

(a) *Direct mode,* $g = 0.65$*,* $Re = 70$*.*

(b) *Adjoint mode,* $g = 0.65$*,* $Re = 70$*.*

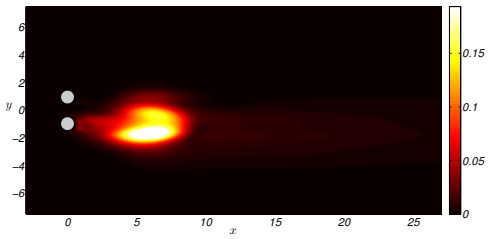

(c) *Structural sensitivity,* $g = 0.65$*,* $Re = 70$*.*

Figure 3.16: *Direct mode*(a)*, adjoint mode* (b) *and structural sensitivity* (c) *related to the far wake mode 5 in the point* $g = 0.65$*,* $Re = 70$*.*

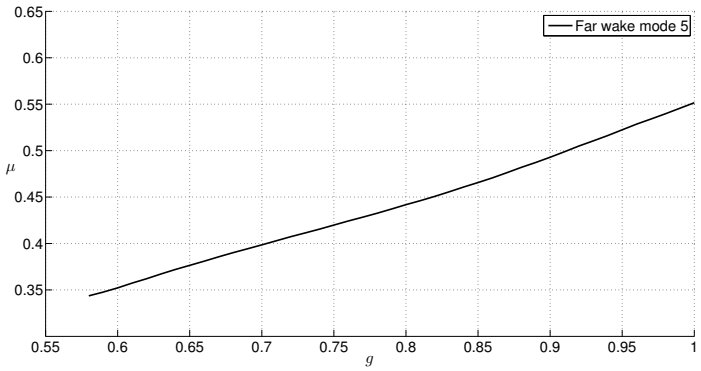

Figure 3.17: *Far wake mode 5:* $\mu = \mu(g)$*.*

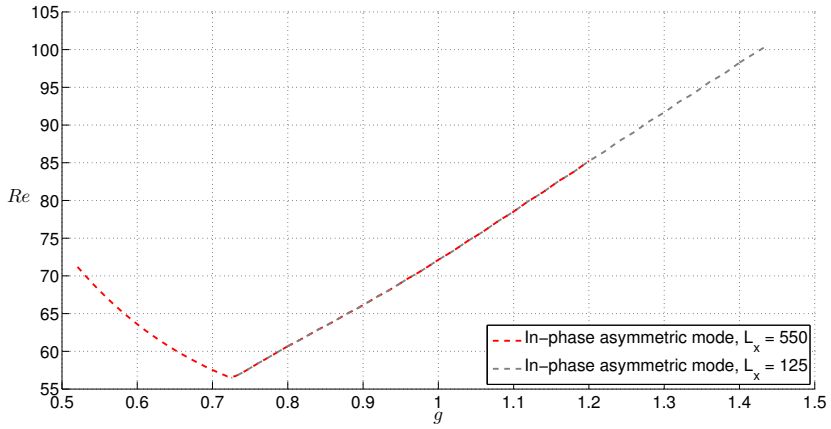

Figure 3.18: *Comparison between the neutral curves associated with the In-phase asymmetric mode computed using two different domain lengths:* $L_x = 550$ *(red curve) and* $L_x = 125$ *(grey curve).*

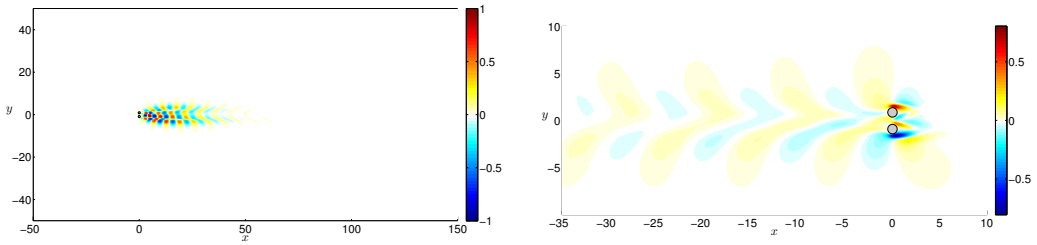

(a) *Direct mode,* $g = 0.77$*,* $Re = 59$*.*

(b) *Adjoint mode,* $g = 0.77$*,* $Re = 59$*.*

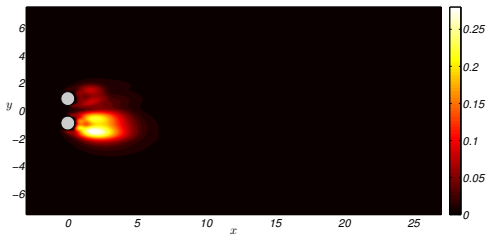

(c) *Structural sensitivity,* $g = 0.77$*,* $Re = 59$*.*

Figure 3.19: *Direct mode*(a)*, adjoint mode* (b) *and structural sensitivity* (c) *related to the In-phase asymmetric mode in the point* $g = 0.77$*,* $Re = 59$*.*

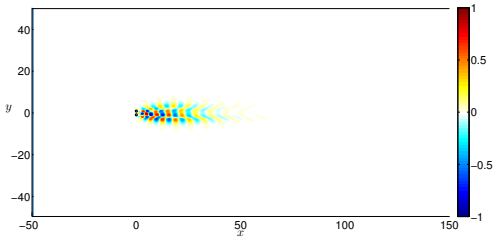

(a) *Direct mode,* $g = 0.8$*,* $Re = 60.75$*.*

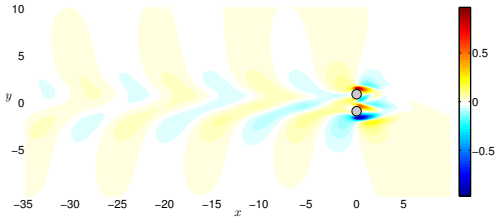

(b) *Adjoint mode,* $g = 0.8$*,* $Re = 60.75$*.*

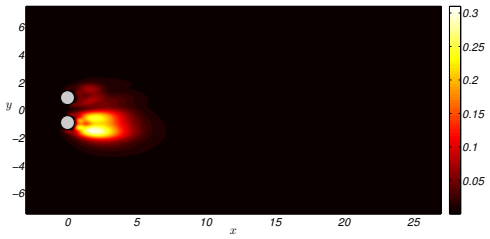

(c) *Structural sensitivity,* $g = 0.8$*,* $Re = 60.75$*.*

Figure 3.20: *Direct mode*(a)*, adjoint mode* (b) *and structural sensitivity* (c) *related to the In-phase asymmetric mode in the point* $g = 0.8$*,* $Re = 60.75$*.*

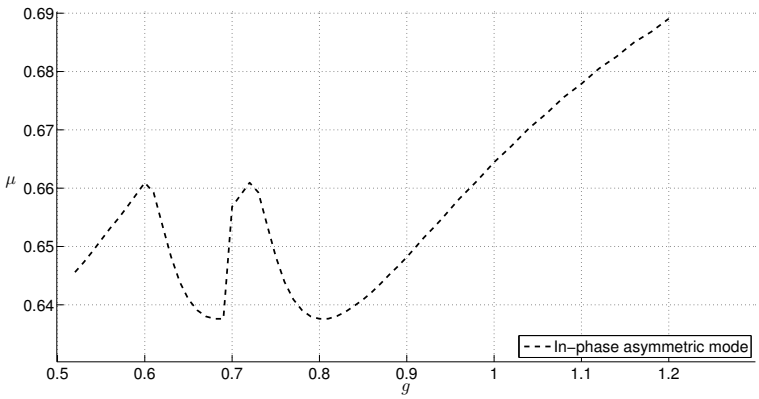

Figure 3.21: *In-phase asymmetric mode:* $\mu = \mu(g)$

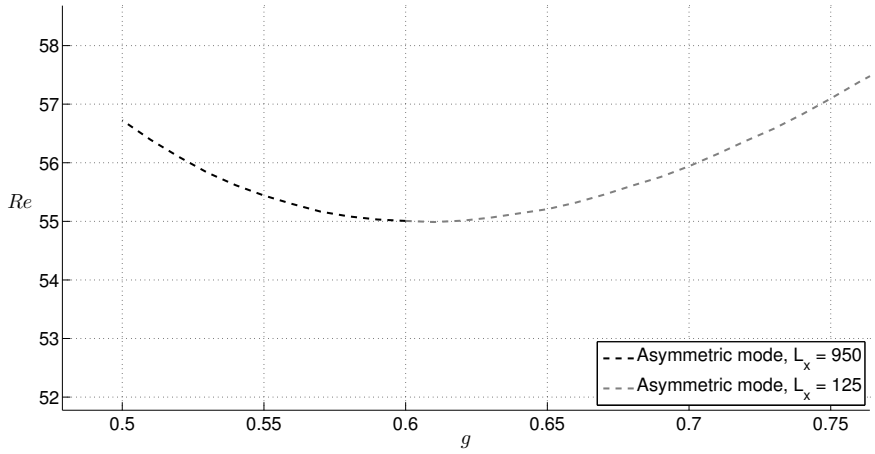

Figure 3.22: *Comparison between the neutral curves associated with the Asymmetric mode computed using two different domain lengths:* $L_x = 950$ *(black curve) and* $L_x = 125$ *(grey curve).*

the lower part of the stability area and it has been verified only for $0.5 < g < 0.6$ using the longest domain ($L_x = 950$), in order to locate the exact points of intersection with the far wake mode 1 and Single Bluff Body mode neutral curves. This curve is different from the others because it is related to a marginally stable real eigenvalue, since it is associated with a pitchfork bifurcation. The curve does not change its shape when a longer domain is used, confirming the accuracy of the results obtained with the shortest domain. In this case, since the eigenvalue which has been tracked is real, its phase, as a function of one of the two parameters, has not been reported.

3.4.4 Single Bluff Body mode

As the previous one, the curve associated with the Single Bluff Body mode has been found by a linear stability analysis on the symmetric base flow. For $Re > 35$, the black curve differs from that computed with the smaller domain, characterised by an almost linear trend with negative slope. For $Re < 35$ the new curve overlaps with that computed with $L_x = 125$. Once again, the curve has been tracked using the longest domain and the corresponding eigenvalue has an imaginary part which varies from $\mu = 0.293$ to $\mu = 0.307$ showing a nearly linear trend.

3.4.5 Far wake mode 1

The blue neutral curve associated with the far wake mode 1 delimits the left part of the stability area. The marginally stable eigenvalue which can be found tracking this curve has a variable frequency close to $\mu = 0.3$ ($0.2971 < \mu < 0.3556$). The curve has been tracked using the longest domain due to the fact that the marginally stable eigenvalue associated with this curve is not converged for $L_x = 550$, as sketched in Figures 3.7 and

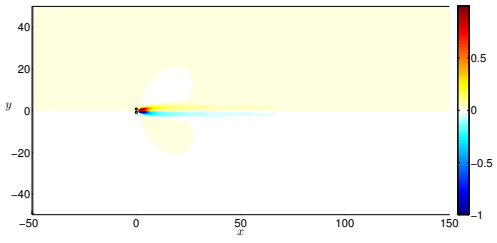

(a) *Direct mode,* $g = 0.56$, $Re = 55.3$.

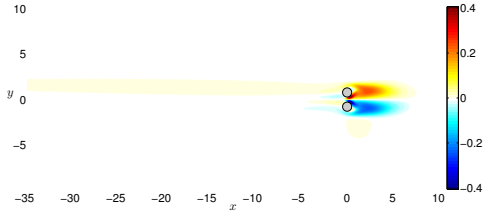

(b) *Adjoint mode,* $g = 0.56$, $Re = 55.3$.

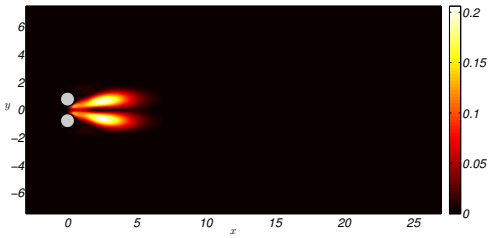

(c) *Structural sensitivity,* $g = 0.56$, $Re = 55.3$.

Figure 3.23: *Direct mode*(a), *adjoint mode* (b) *and structural sensitivity* (c) *related to the Asymmetric mode in the point* $g = 0.56$, $Re = 55.3$.

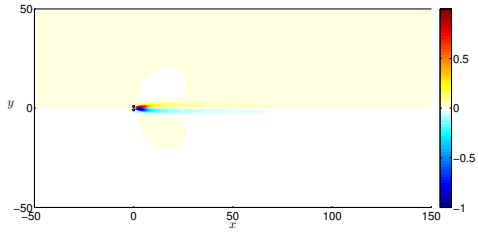

(a) *Direct mode,* $g = 0.67$, $Re = 55.5$.

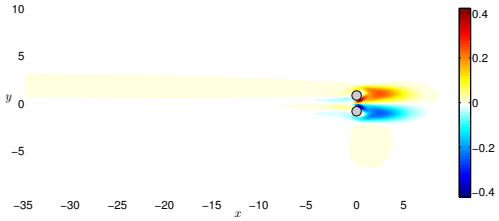

(b) *Adjoint mode,* $g = 0.67$, $Re = 55.5$.

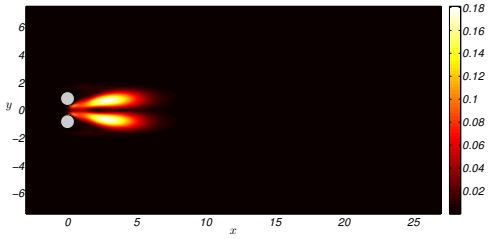

(c) *Structural sensitivity,* $g = 0.67$, $Re = 55.5$.

Figure 3.24: *Direct mode*(a), *adjoint mode* (b) *and structural sensitivity* (c) *related to the Asymmetric mode in the point* $g = 0.67$, $Re = 55.5$.

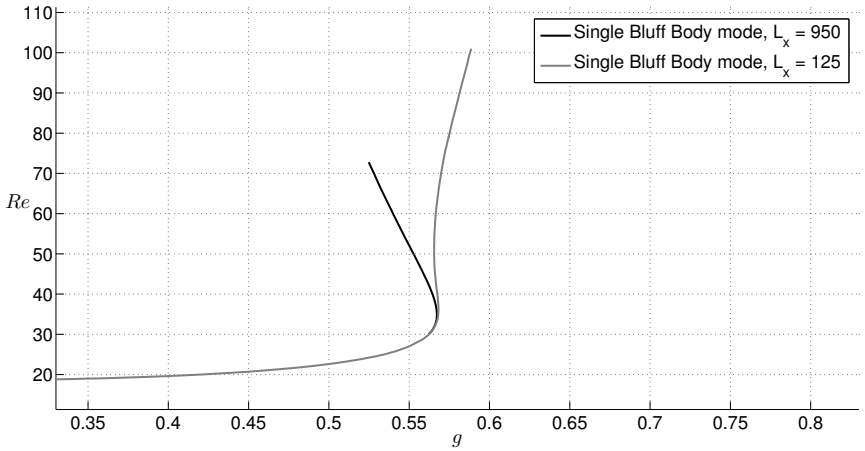

Figure 3.25: *Comparison between the neutral curves associated with the Single-Bluff Body mode computed using two different domain lengths:* $L_x = 950$ *(black curve) and* $L_x = 125$ *(grey curve).*

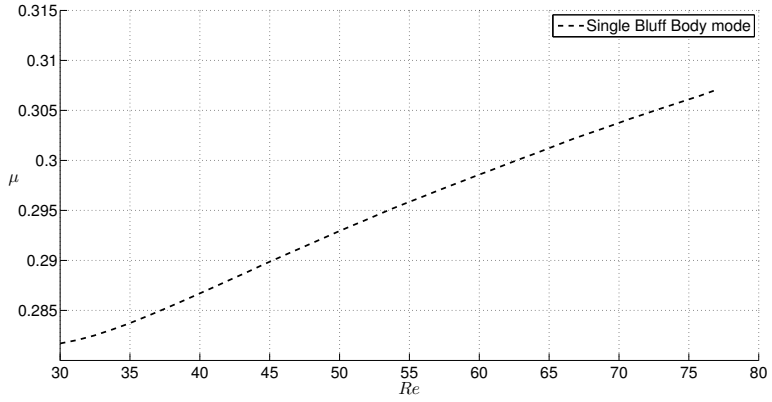

Figure 3.26: *Single Bluff Body mode:* $\mu = \mu(Re)$.

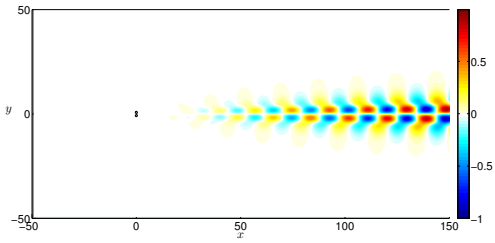

(a) *Direct mode,* $g = 0.56$, $Re = 44$.

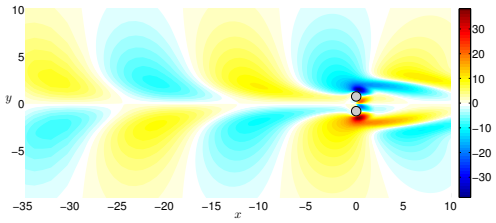

(b) *Adjoint mode,* $g = 0.56$, $Re = 44$.

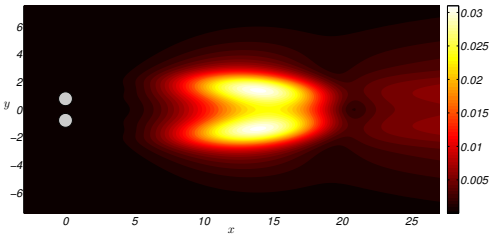

(c) *Structural sensitivity,* $g = 0.56$, $Re = 44$.

Figure 3.27: *Direct mode*(a), *adjoint mode* (b) *and structural sensitivity* (c) *related to the Single Bluff Body mode in the point* $g = 0.56$, $Re = 44$.

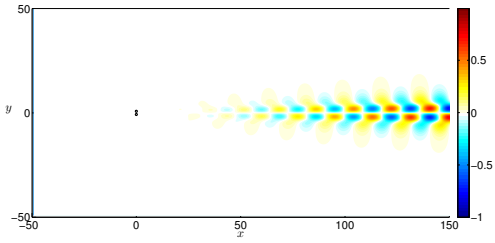

(a) *Direct mode,* $g = 0.55$, $Re = 52$.

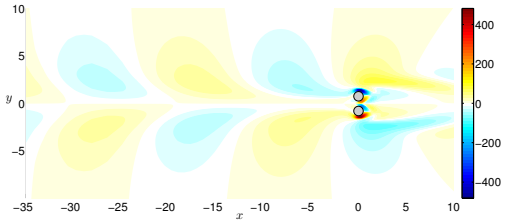

(b) *Adjoint mode,* $g = 0.55$, $Re = 52$.

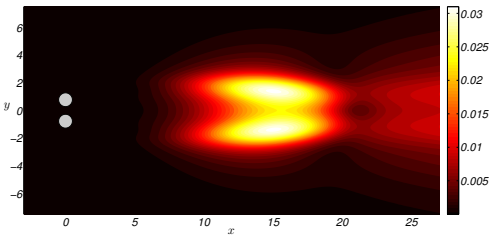

(c) *Structural sensitivity,* $g = 0.55$, $Re = 52$.

Figure 3.28: *Direct mode*(a), *adjoint mode* (b) *and structural sensitivity* (c) *related to the Single Bluff Body mode in the point* $g = 0.55$, $Re = 52$.

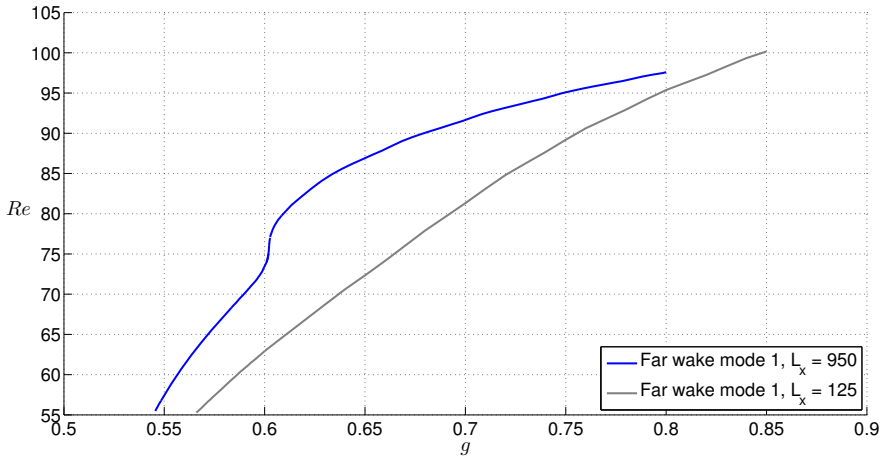

Figure 3.29: *Comparison between the neutral curves associated with the far wake mode 1 computed using two different domain lengths:* $L_x = 950$ *(blue curve) and* $L_x = 125$ *(grey curve).*

3.8. These plots also show how a domain length $L_x \geq 900$ is required to correctly track this marginally stable eigenvalue in the parameter space.
With respect to the curve computed on the shorter domain, the new neutral curve is placed at higher Reynolds numbers. The slope, $\frac{dRe}{dg}$, is higher and for $57 < Re < 70$ it displays an almost linear trend; for $Re > 70$, the curve behaviour changes: for $Re \approx 75$ the curve has a knee and for higher Reynolds number $\frac{d^2Re}{dg^2} < 0$. This neutral curve is the most difficult to track from a computational point of view, since the continuation algorithm converged only for small steps. A continuation step of $Re = 0.05$ has been employed to reproduce the portion $70 < Re < 80$.
The curve has been continued until its end for low Re and g, where it intersects the neutral curve of the Single-bluff-body mode.

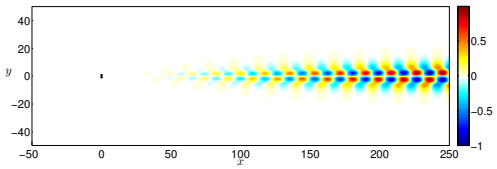

(a) *Direct mode,* $g = 0.558$, $Re = 60.5$.

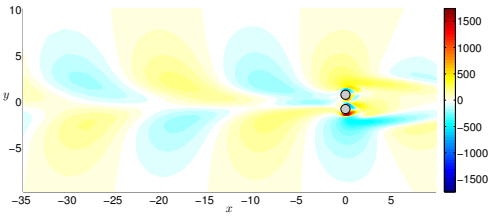

(b) *Adjoint mode,* $g = 0.558$, $Re = 60.5$.

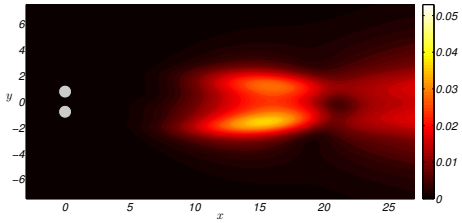

(c) *Structural sensitivity,* $g = 0.558$, $Re = 60.5$.

Figure 3.30: *Direct mode*(a), *adjoint mode* (b) *and structural sensitivity* (c) *related to the far wake mode 1 in the point* $g = 0.558$, $Re = 60.5$.

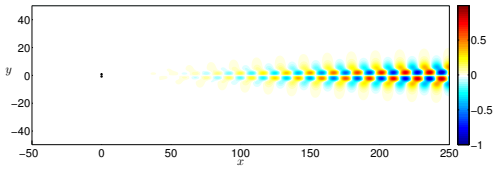

(a) *Direct mode,* $g = 0.595$, $Re = 71.5$.

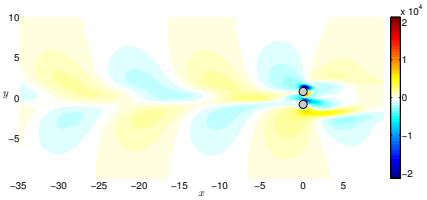

(b) *Adjoint mode,* $g = 0.595$, $Re = 71.5$.

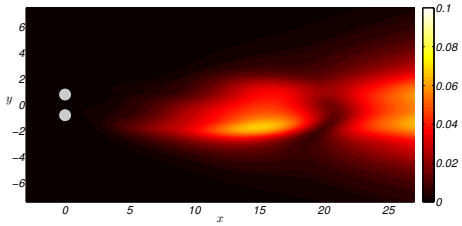

(c) *Structural sensitivity,* $g = 0.595$, $Re = 71.5$.

Figure 3.31: *Direct mode*(a), *adjoint mode* (b) *and structural sensitivity* (c) *related to the far wake mode 1 in the point* $g = 0.595$, $Re = 71.5$.

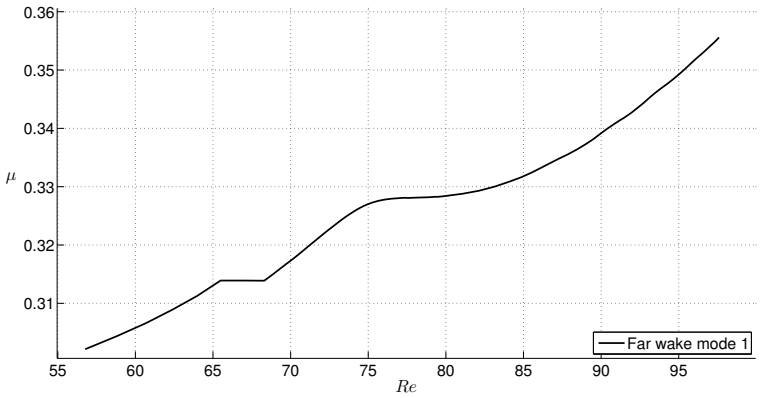

Figure 3.32: *Far wake mode 1:* $\mu = \mu(Re)$.

3.4.6 Single-shedding mode

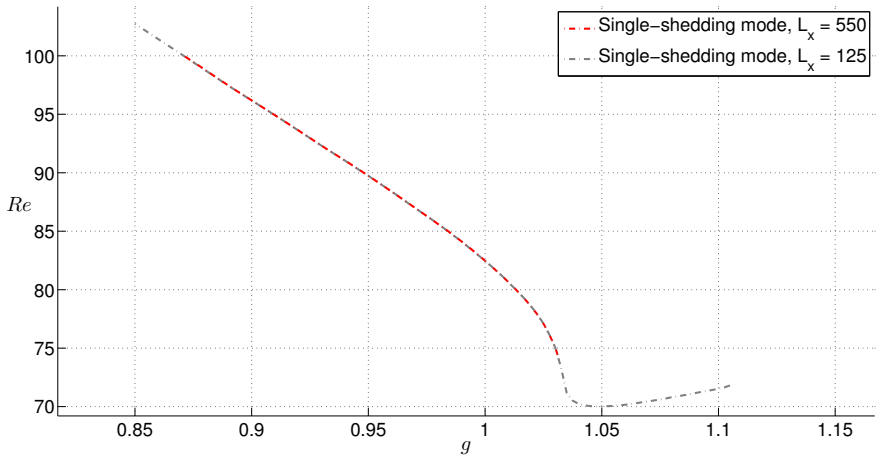

Figure 3.33: *Comparison between the neutral curves associated with the Single-shedding mode computed using two different domain lengths:* $L_x = 550$ *(red curve) and* $L_x = 125$ *(grey curve).*

The neutral curve associated with the Single-shedding mode does not contribute to define the boundary of the stability area, for this reason it covers a secondary role in this work. However, its trend has been accurately tracked to locate any possible point of intersection with the far wake mode 5, once the domain has been lengthened. It is easy to note how this curve has not changed its position in the parameter space once the domain length has been increased and therefore it still intersects the neutral curve associated with the In-phase asymmetric mode in the same point found using the shorter domain.
The imaginary part of the eigenvalue related to this curve and spans a range of values from $\mu = 0.972$ to $\mu = 1.084$. The curve has been drawn using a length of $L_x = 550$.

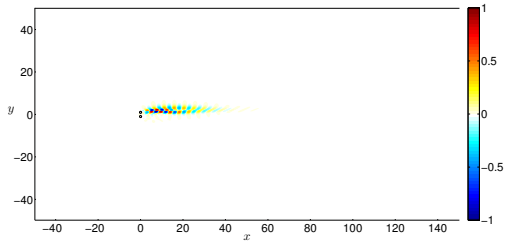

(a) *Direct mode,* $g = 0.97$, $Re = 87$.

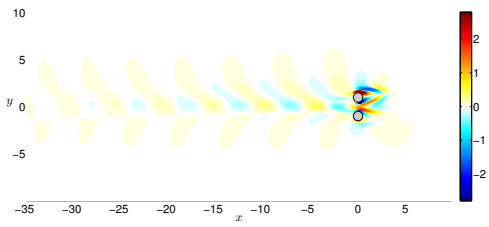

(b) *Adjoint mode,* $g = 0.97$, $Re = 87$.

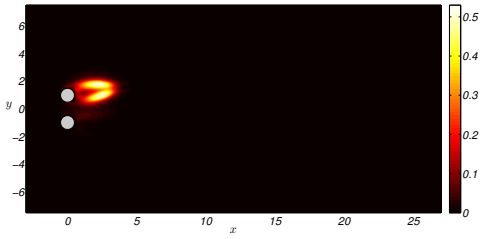

(c) *Structural sensitivity,* $g = 0.97$, $Re = 87$.

Figure 3.34: *Direct mode*(a)*, adjoint mode* (b) *and structural sensitivity* (c) *related to the Single-shedding mode in the point* $g = 0.97$, $Re = 87$.

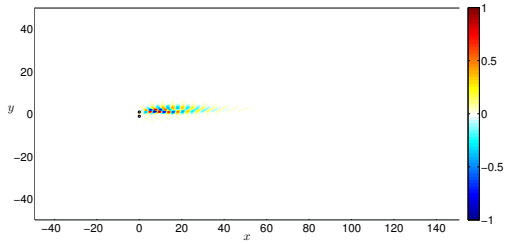

(a) *Direct mode,* $g = 1$, $Re = 83$.

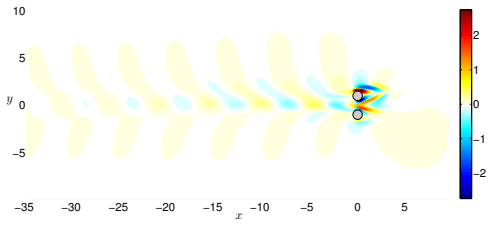

(b) *Adjoint mode,* $g = 1$, $Re = 83$.

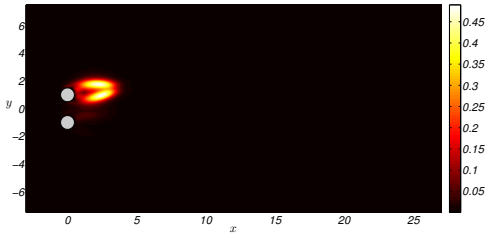

(c) *Structural sensitivity,* $g = 1$, $Re = 83$.

Figure 3.35: *Direct mode*(a)*, adjoint mode* (b) *and structural sensitivity* (c) *related to the Single-shedding mode in the point* $g = 1$, $Re = 83$.

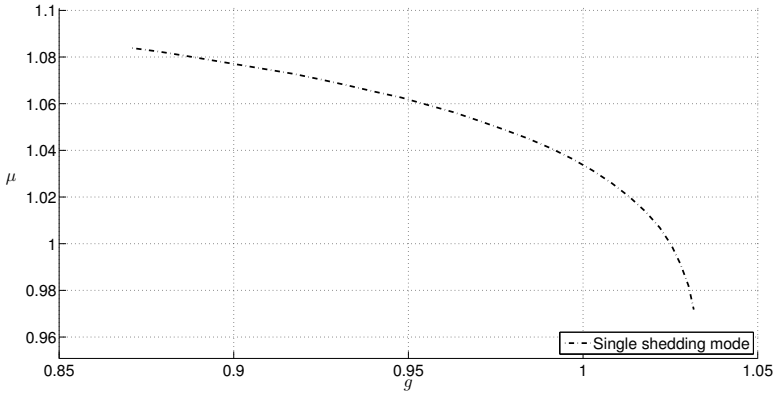

Figure 3.36: *Single Shedding mode:* $\mu = \mu(g)$.

3.5 Stability area definition

Once all the neutral curves have been tracked, the stability area has been reconstructed. Figure 3.37 reports an overall view of the neutral curves depicted in the parameter space. The curves which are related to the symmetric base flow are those calculated by Carini, with the exception of that associated with the Single Bluff Body mode which has been re-defined with the lengthened domain. The asymptotic stability area has been marked in yellow. It is enclosed by the five neutral curves described above, with the exception of that associated with the Single-shedding mode. The points of intersection between the different curves are codimension-two bifurcation points, *i.e.* in these points two independent eigenvalues simultaneously cross the imaginary axis, leading to an unstable flow. The local minimum of the In-phase asymmetric mode represents the intersection of three neutral curves, also this is a codimension-two bifurcation point since one of the bifurcations concerns the asymmetric baseflow.

In Figure 3.39 the stability area, obtained with a domain length of $L_x = 125$ and depicted in green, is compared with that computed in the present work. The new stability area is more extended. Taking the codimension-two bifurcation point as a reference, it is easy to observe how the large-gap portion of the stable region in the parameter space does not change shape using the lengthened domain. In fact, for large gap, the neutral curves overlap almost perfectly. However, the left part of the stability region changes significantly: first of all the cusp in the point $g \approx 0.75$, $Re = 69.1$ is no longer present; furthermore, the shape of the far wake mode 5 changes extending the stability region towards higher Reynolds numbers; in addition, the increasing of the slope related to the neutral curve associated with the Far wake mode 1 has expanded the left boundary towards lower gaps, while the different path followed by the Single Bluff Body mode has modified the left lower corner of the area. Moreover, looking at the neutral curve associated with the Far wake mode 1, the portion of the neutral curve between $70 < Re < 80$ corresponds to the intersection with the continuous neutral curve associated with the Far wake mode

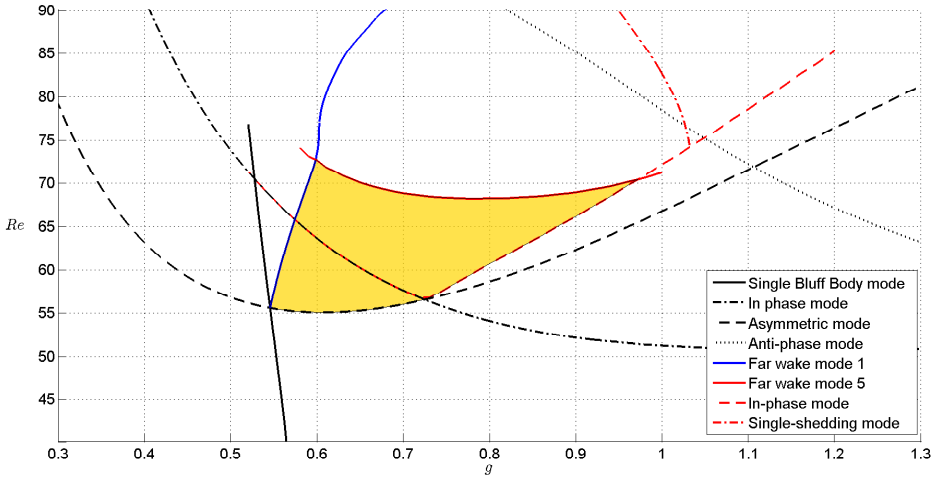

Figure 3.37: *Neutral curves in the parameter space calculated using different domain sizes. The curves associated with the far wake mode 5, In-phase asymmetric mode and Single-shedding mode have been tracked using a domain length $L_x = 550$. The curves associated with the Single Bluff Body mode and the far wake mode 1 have been calculated employing a domain size $L_x = 950$. The remaining neutral curves are those calculated by Carini using a domain extension equal to $L_x = 125$. The yellow zone represents the new stability area of the asymmetric base flow.*

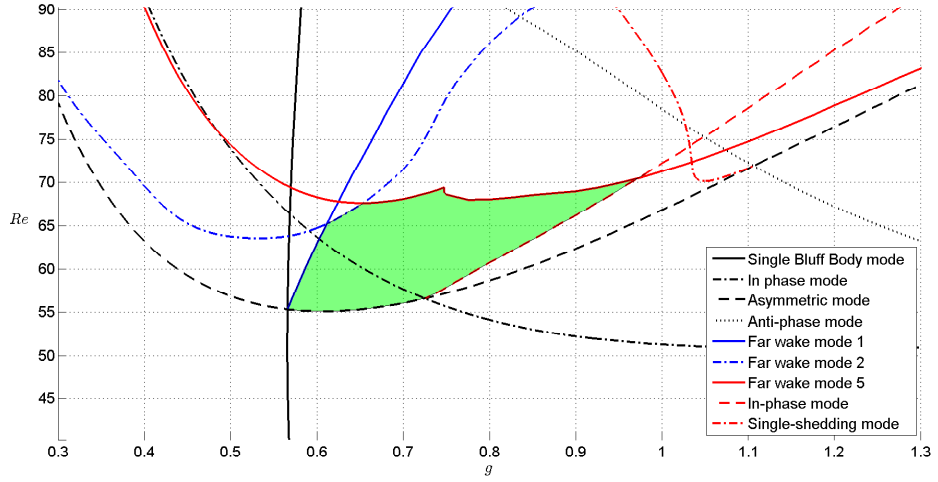

Figure 3.38: *Neutral curves in the parameter space calculated by M. Carini [10] using a domain length of $L_x = 125$. The green zone represents the stability area of the asymmetric base flow.*

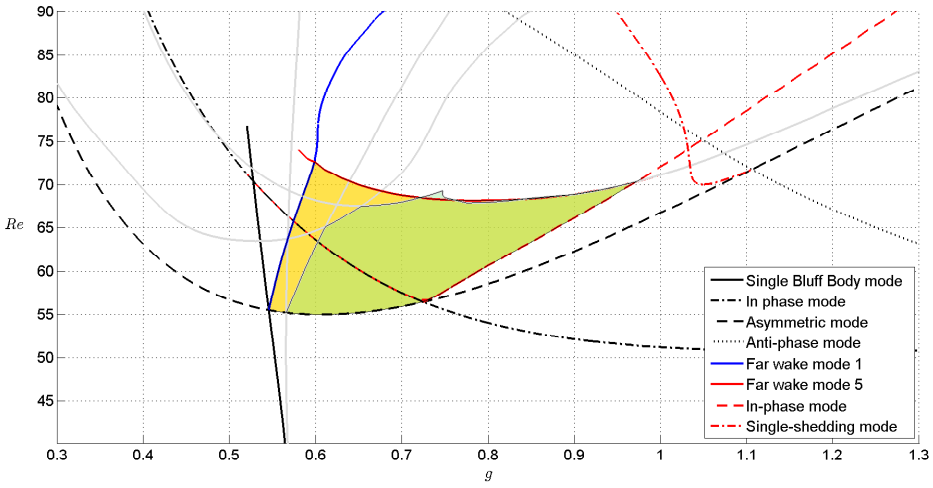

Figure 3.39: *Comparison of the stability regions for the asymmetric base flow in the parameter space traced in the present work with that calculated by M. Carini [10] (green). The difference is coloured in yellow. The grey neutral curves represent the neutral curves traced in [10].*

1. The explanantion of such a great difficulty in tracking this segment, may be found looking at the trend of μ with respect to the Reynolds number: in fact the imaginary parts of the two eigenvaues are very similar to each other. This may be a problem for the continuation algorithm, that does not recognize the correct neutral curve that must be tracked. In addition, the nonlinear behaviour of the neutral curve associated with the Far wake mode 1 in the neighbourhood of that point, could make the neutral curve tracking more complicated.

3.6 DNS results

The last section of the chapter is concerned with the results obtained by a set of thirteen DNSs which have been performed to assess the information obtained by the linear stability analysis. These simulations have been performed in different points of the parameter space, placed across the neutral curves which delimit the stability area of the asymmetric base flow. Figure 3.40 reports the position of the points, with the corresponding values of Reynolds number and adimensional gap spacing.

The points are organised in pairs: each pair is placed across a specific neutral curve, in order to check the stability properties of the flow inside and outside of the stability area. The only point which does not have an equivalent one in the unstable zone, is the point $Re = 62.5$, $g = 0.7$ that has been placed in the central part of the stable zone.

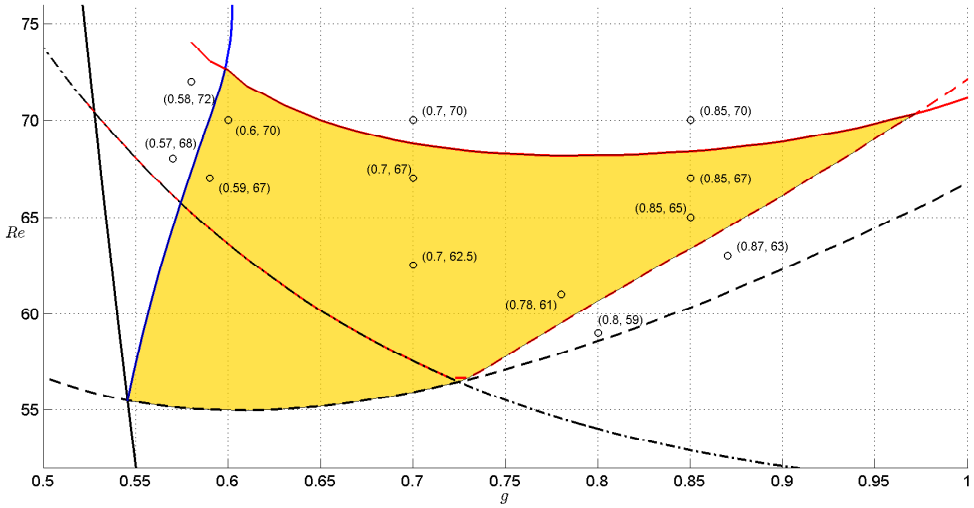

Figure 3.40: *Points in the parameter space in which the different DNSs have been performed.*

Moreover, parameters used for the simulations have not been chosen too close to the critical values, to avoid excessively long calculations: in fact near the neutral curves, the growth rate of the unstable mode, quantified by the real part of the eigenvalue of interest, vanishes as the neutral curve is approached. This means that if the simulation starts from a slightly perturbed condition, the instability manifests itself after a very long time requiring significant computational resources. The employed code, can be used with two different time integration schemes: a Crank-Nicolson/Runge-Kutta scheme and a Crank-Nicolson/Adam-Bashforth-2 scheme; the latter has been chosen because it assured a faster execution time notwithstanding the reduced time-step size. Moreover, the first one would have been too onerous from a computational point of view, since it requires a larger quantity of RAM. The time step of the simulations has been set to $\Delta t = 0.005$ while the final time has been fixed to $T = 500$. However, for some simulations, the final time has been extended up to $T = 1000$ in order to allow the instability to produce appreciable effects. The perturbed base flow has been used as initial condition. The simulations have been performed using two different domain lenghts, using the same size employed to reconstruct the neutral curves. In particular, DNSs illustrated in Figures 3.49-3.52 have been performed using a domain length of $L_x = 950$ since they are placed near the neutral curve associated with the Far-wake mode 1. The other simulations have been carried out using a domain length $L_x = 550$. The DNSs confirm the results obtained by the linear stability analysis.

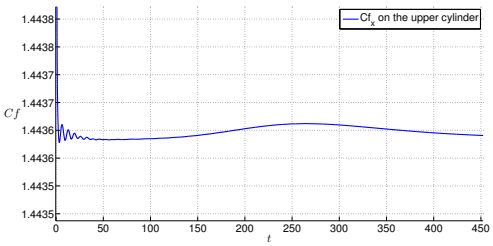

(a) *Upper cylinder:* $C_f = C_f(t)$, $g = 0.7$, $Re = 67$.

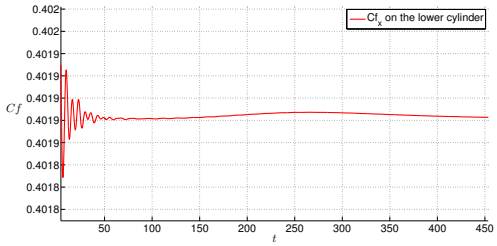

(b) *Lower cylinder:* $C_f = C_f(t)$, $g = 0.7$, $Re = 67$.

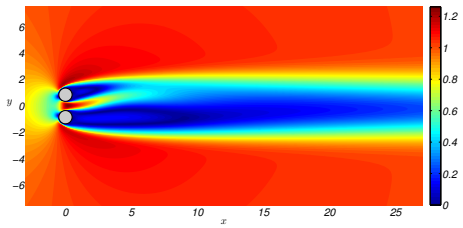

(c) *Flow at* $t = 500$.

Figure 3.41: *Aerodynamic coefficients of the upper* (a) *and lower* (b) *cylinders as a function of time at* $g = 0.7$, $Re = 67$. *The subfigure* (c) *shows the flow at the final time instant. The base flow is stable.*

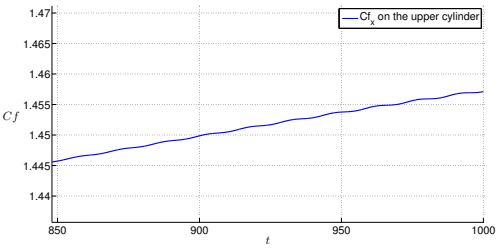

(a) *Upper cylinder:* $C_f = C_f(t)$, $g = 0.7$, $Re = 70$.

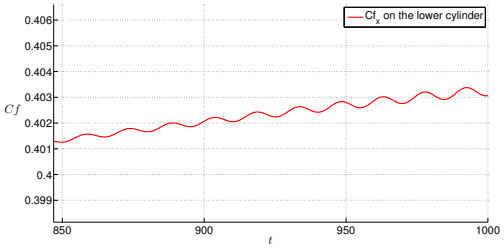

(b) *Lower cylinder:* $C_f = C_f(t)$, $g = 0.7$, $Re = 70$.

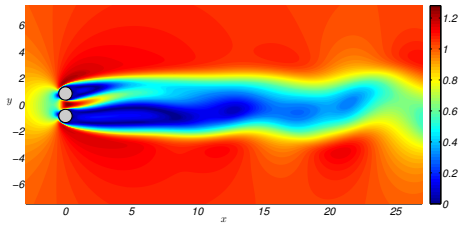

(c) *Flow at* $t = 1000$.

Figure 3.42: *Aerodynamic coefficients of the upper* (a) *and lower* (b) *cylinders as a function of time at* $g = 0.7$, $Re = 70$. *The subfigure* (c) *shows the flow at the final time instant. The base flow is unstable.*

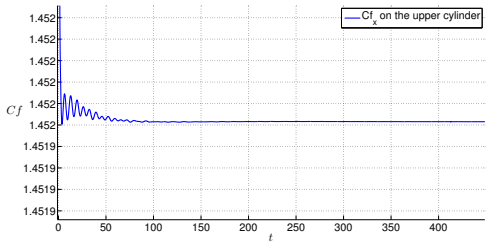

(a) *Upper cylinder:* $C_f = C_f(t)$, $g = 0.85$, $Re = 67$.

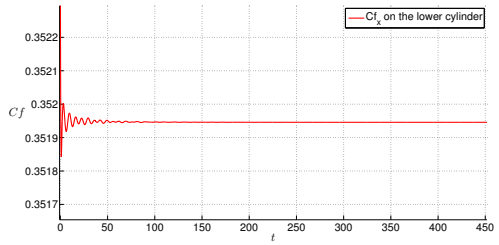

(b) *Lower cylinder:* $C_f = C_f(t)$, $g = 0.85$, $Re = 67$.

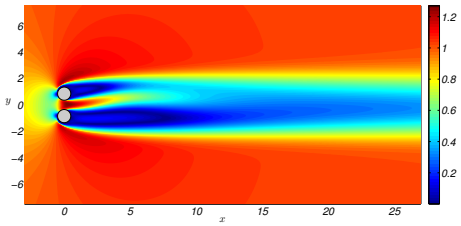

(c) *Flow at* $t = 500$.

Figure 3.43: *Aerodynamic coefficients of the upper* (a) *and lower* (b) *cylinders as a function of time at* $g = 0.85$, $Re = 67$. *The subfigure* (c) *shows the flow at the final time instant. The base flow is stable.*

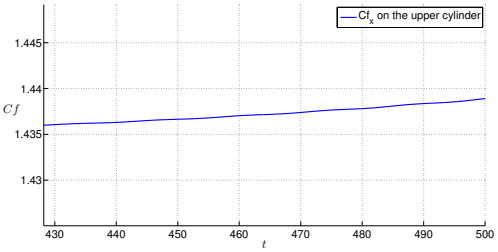

(a) *Upper cylinder:* $C_f = C_f(t)$, $g = 0.85$, $Re = 70$.

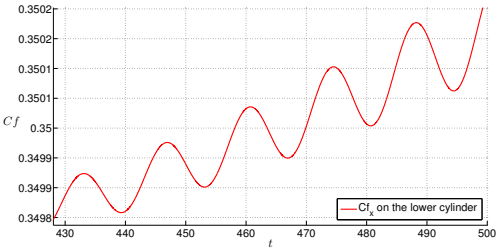

(b) *Lower cylinder:* $C_f = C_f(t)$, $g = 0.85$, $Re = 70$.

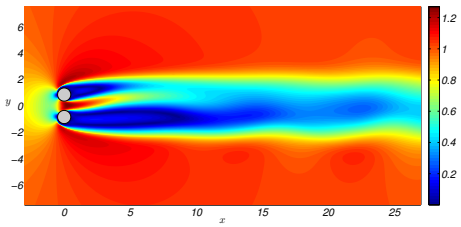

(c) *Flow at* $t = 500$.

Figure 3.44: *Aerodynamic coefficients of the upper* (a) *and lower* (b) *cylinders as a function of time at* $g = 0.85$, $Re = 70$. *The subfigure* (c) *shows the flow at the final time instant. The base flow is unstable.*

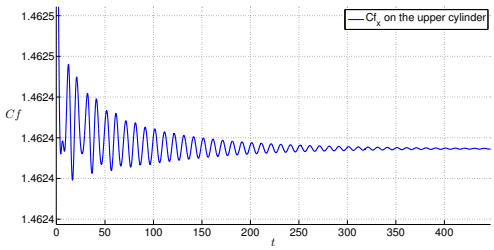

(a) *Upper cylinder:* $C_f = C_f(t)$, $g = 0.85$, $Re = 65$.

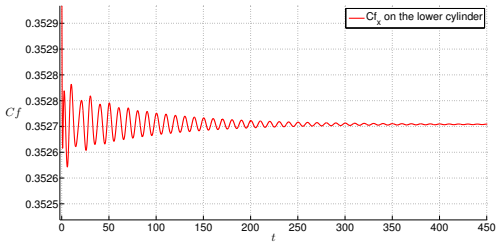

(b) *Lower cylinder:* $C_f = C_f(t)$, $g = 0.85$, $Re = 65$.

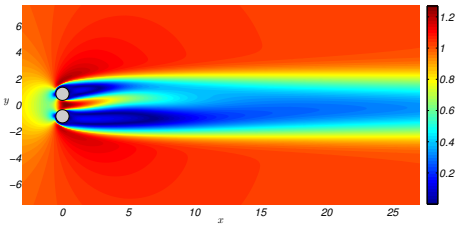

(c) *Flow at* $t = 500$.

Figure 3.45: *Aerodynamic coefficients of the upper* (a) *and lower* (b) *cylinders as a function of time at* $g = 0.85$, $Re = 65$. *The subfigure* (c) *shows the flow at the final time instant. The base flow is stable.*

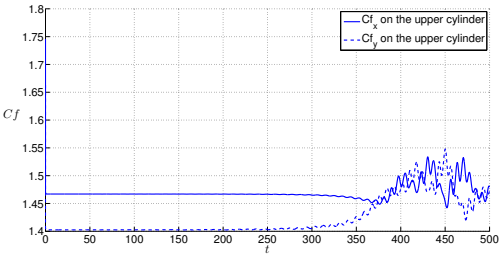

(a) *Upper cylinder:* $C_f = C_f(t)$, $g = 0.87$, $Re = 63$.

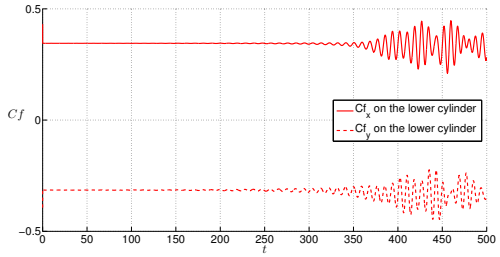

(b) *Lower cylinder:* $C_f = C_f(t)$, $g = 0.87$, $Re = 63$.

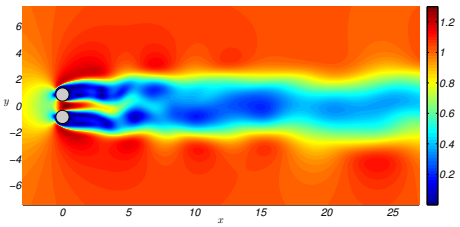

(c) *Flow at* $t = 500$.

Figure 3.46: *Aerodynamic coefficients of the upper* (a) *and lower* (b) *cylinders as a function of time at* $g = 0.87$, $Re = 63$. *The subfigure* (c) *shows the flow at the final time instant. The base flow is unstable.*

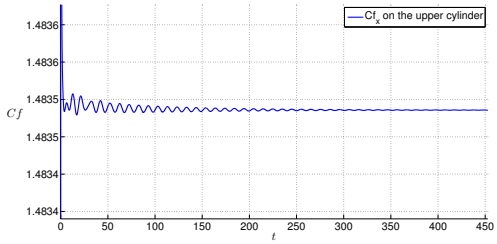

(a) *Upper cylinder:* $C_f = C_f(t)$, $g = 0.78$, $Re = 61$.

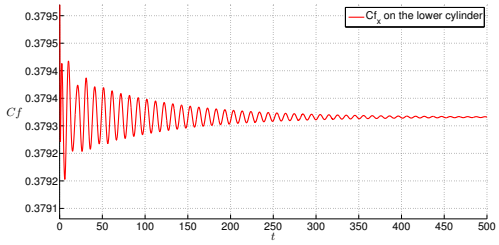

(b) *Lower cylinder:* $C_f = C_f(t)$, $g = 0.78$, $Re = 61$.

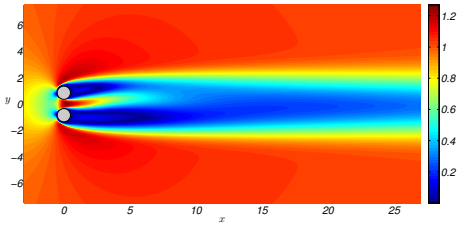

(c) *Flow at* $t = 500$.

Figure 3.47: *Aerodynamic coefficients of the upper* (a) *and lower* (b) *cylinders as a function of time at* $g = 0.78$, $Re = 61$. *The subfigure* (c) *shows the flow at the final time instant. The base flow is stable.*

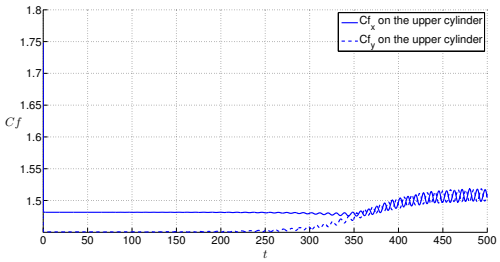

(a) *Upper cylinder:* $C_f = C_f(t)$, $g = 0.8$, $Re = 59$.

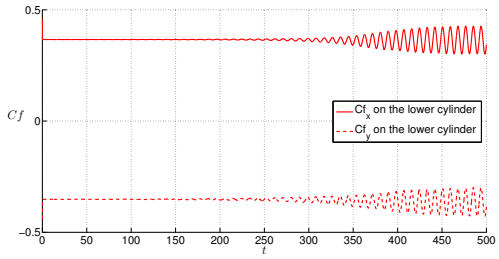

(b) *Lower cylinder:* $C_f = C_f(t)$, $g = 0.8$, $Re = 59$.

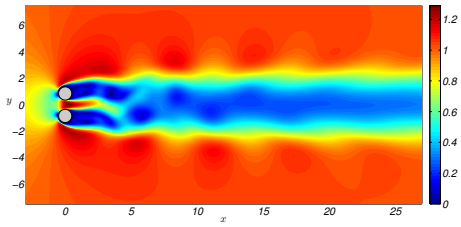

(c) *Flow at* $t = 500$.

Figure 3.48: *Aerodynamic coefficients of the upper* (a) *and lower* (b) *cylinders as a function of time at* $g = 0.8$, $Re = 59$. *The subfigure* (c) *shows the flow at the final time instant. The base flow is unstable.*

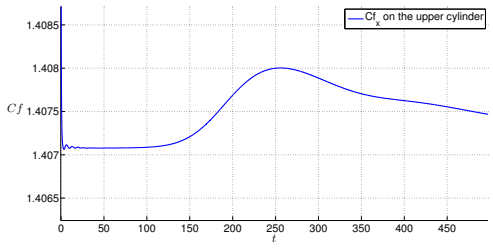

(a) *Upper cylinder:* $C_f = C_f(t)$, $g = 0.6$, $Re = 70$.

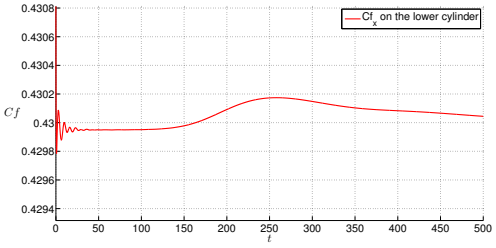

(b) *Lower cylinder:* $C_f = C_f(t)$, $g = 0.6$, $Re = 70$.

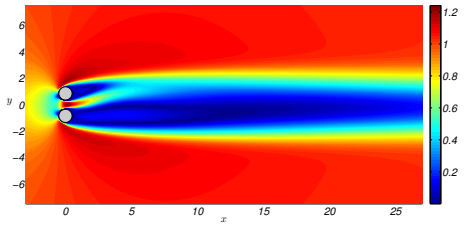

(c) *Flow at* $t = 500$.

Figure 3.49: *Aerodynamic coefficients of the upper* (a) *and lower* (b) *cylinders as a function of time at* $g = 0.6$, $Re = 70$. *The subfigure* (c) *shows the flow at the final time instant. The base flow is stable.*

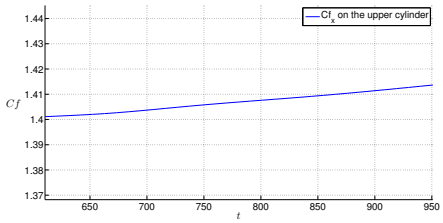

(a) *Upper cylinder:* $C_f = C_f(t)$, $g = 0.58$, $Re = 72$.

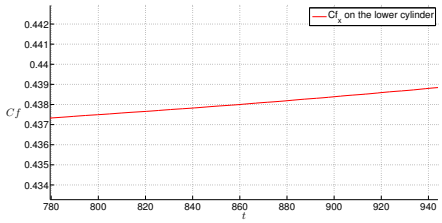

(b) *Lower cylinder:* $C_f = C_f(t)$, $g = 0.58$, $Re = 72$.

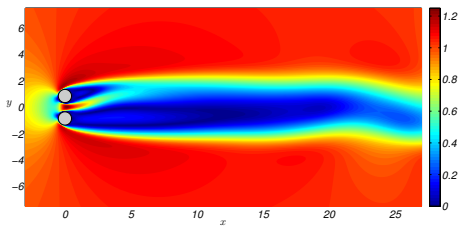

(c) *Flow at* $t = 1000$.

Figure 3.50: *Aerodynamic coefficients of the upper* (a) *and lower* (b) *cylinders as a function of time at* $g = 0.58$, $Re = 72$. *The subfigure* (c) *shows the flow at the final time instant. The base flow is unstable.*

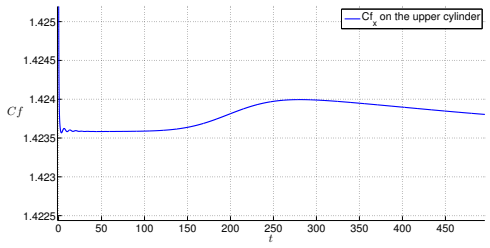

(a) *Upper cylinder:* $C_f = C_f(t)$, $g = 0.59$, $Re = 67$.

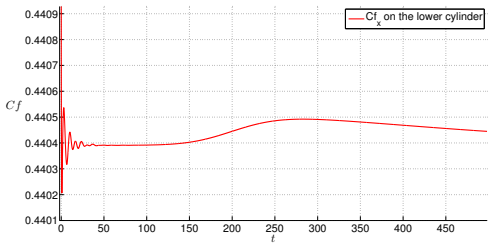

(b) *Lower cylinder:* $C_f = C_f(t)$, $g = 0.59$, $Re = 67$.

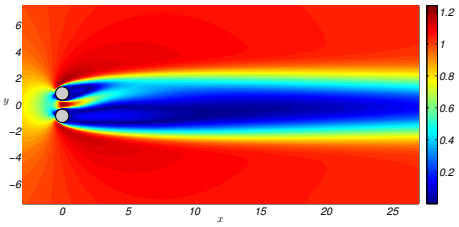

(c) *Flow at* $t = 500$.

Figure 3.51: *Aerodynamic coefficients of the upper* (a) *and lower* (b) *cylinders as a function of time at* $g = 0.59$, $Re = 67$. *The subfigure* (c) *shows the flow at the final time instant. The base flow is stable.*

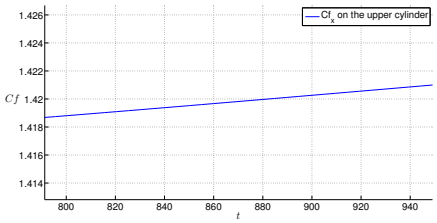

(a) *Upper cylinder:* $C_f = C_f(t)$, $g = 0.57$, $Re = 68$.

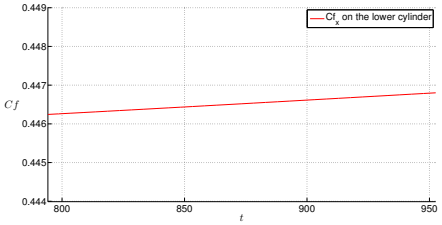

(b) *Lower cylinder:* $C_f = C_f(t)$, $g = 0.57$, $Re = 68$.

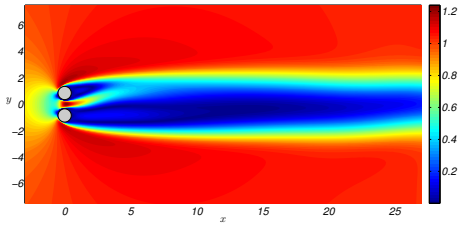

(c) *Flow at* $t = 1000$.

Figure 3.52: *Aerodynamic coefficients of the upper* (a) *and lower* (b) *cylinders as a function of time at* $g = 0.57$, $Re = 68$. *The subfigure* (c) *shows the flow at the final time instant. The base flow is unstable.*

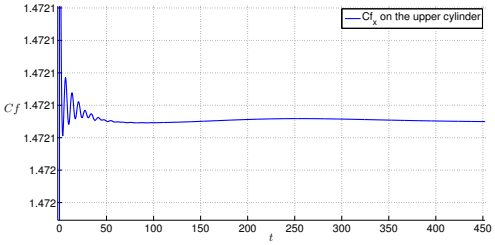

(a) *Upper cylinder:* $C_f = C_f(t)$, $g = 0.7$, $Re = 62.5$.

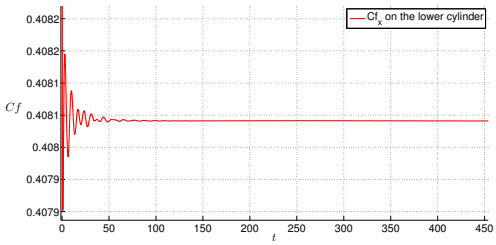

(b) *Lower cylinder:* $C_f = C_f(t)$, $g = 0.7$, $Re = 62.5$.

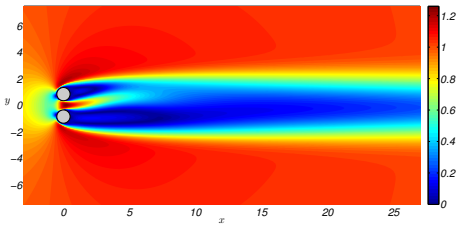

(c) *Flow at* $t = 500$.

Figure 3.53: *Aerodynamic coefficients of the upper* (a) *and lower* (b) *cylinders as a function of time at* $g = 0.7$, $Re = 62.5$. *The subfigure* (c) *shows the flow at the final time instant. The base flow is stable.*

CHAPTER 4

Conclusions and future works

In the present work, the linear stability analysis of the steady asymmetric base flow around two circular cylinders in side-by-side arrangement has been investigated.
The dynamics of the flow has been numerically studied as a function of the two parameters that govern the physics of the problem, *i.e.* the Reynolds number Re and the adimensional gap spacing g.
The steady, incompressible Navier–Stokes equations have been used to model the viscous flow around the two cylinders and have been linearized to perform the linear stability analysis. An immersed boundary method has been used to discretize the problem, thus avoiding any change to the mesh when the gap spacing between the cylinders is varied. The study has been performed using a software package written in the CPL language by Flavio Giannetti. The code has been carefully validated, by comparison with reference results about the flow past a cylinder, both still and rotating.
The first part of the analysis has been devoted to identify the minimum domain length for which the eigenvalues are converged. Meanwhile, the calculation of the structural sensitivity of the marginally stable mode has been computed in order to locate the most unstable area within the flow. In the second step of the work, the considered domain has been used to re-define the neutral curves which delimit the stability area of the asymmetric base flow, comparing present results with the ones reported by M. Carini in [10].
The investigation started from the point $Re = 68$, $g = 0.7$ in the parameter space to better understand the behaviour of the marginally stable eigenvalue associated with the far wake mode 5, which delimits the upper boundary of the stability area. The results have shown that a domain length $L_x = 550$ diameters assures a good convergence of the above-mentioned eigenvalue, up to four significant digits. In contrast, this length is not adequate to reproduce the neutral curves which define the left boundary of the stability area, in particular the curves associated with the Far-wake mode 1 and Single-bluff-body

mode. In this case, a dimension $L_x = 950$ diameters is required. For what concerns the structural sensitivity, its maximum, *i.e.* the "wavemaker", is located behind the lower cylinder, near the bigger recirculation bubble.
The results found in the second part of the analysis underline that the left part of the stability area is the most sensitive to the domain length: in fact, the neutral curves associated with the far wake mode 1 and Single Bluff Body mode change significantly when the domain is lengthened, extending the stability region toward higher Reynolds numbers and lower gap spacing. In particular, large changes have been observed in the neutral curve associated with the far wake 1 mode. This curve has been the most difficult one to track and a continuation step of 0.05 in Reynolds number has been used to reproduce the portion in the interval $70 < Re < 80$. The right-hend part of the stability area does not change using extended domains.
For the first time, the sensitivity of the least stable eigenvalues, with respect to the length of the numerical domain has been investigated. In fact, the least stable eigenvalues and the associated neutral curves, which delimit the asymptotical stability area in the parameter space (g, Re), are quite sensitive to the domain size for low gap spacing. The present investigation allow one to conclude that the stability area calculated by M. Carini [10] was not accurate, since a too short domain was used.
A set of DNSs has been carried out to validate the results of the stability analysis: the points in the parameter space for which the simulations have been run are placed across the neutral curves of interest to check the stability and instability properties of the flow. The results obtained by the DNSs fully agree with those of the linear stability study: in fact, after a transient phase, the aerodynamic coefficients for flows with parameters belonging to the stability area, show a stable behaviour. On the other hand, the simulations performed outside the stability area, underline an unstable trend of the aerodynamic forces, which diverge from the equilibrium solution.
Further studies should be completed to fully understand the different mechanisms which govern the stability of this flow. Possible developments could include:

- a nonlinear analysis of the codimension-two bifurcation points which represent the corners of the stability area to fully unveil the phase portait of the flow;
- a full redefinition of all the neutral curves in the purple area depicted in Figure 0.2, using the extended domains.

APPENDIX A

Estratto in italiano

Introduzione La simulazione di flussi viscosi attorno a corpi tozzi è uno dei problemi di maggior interesse in ambito scientifico: l'attenzione nasce dal fatto che in questi tipi di flussi sono presenti molti fenomeni basilari di natura fluidodinamica, come la separazione dello strato limite la formazione di scie instazionarie, la transizione alla turbolenza. Inoltre, a livello pratico, lo studio dell'aerodinamica di strutture quali piloni di ponti, grattacieli o scambiatori di calore è molto comune nel campo dell'ingegneria civile ed energetica e può essere effettuato mediante tecniche numeriche.
In particolare, una configurazione che negli ultimi anni è stata analizzata con interesse è quella di due cilindri affiancati sotto l'azione di una corrente uniforme, come dimostrano i molti esempi presenti in letteratura. Uno degli aspetti che caratterizza maggiormente questa corrente, a bassi numeri di Reynolds, è la presenza di due correnti stazionarie, una simmetrica e l'altra asimmetrica, con caratteristiche di stabilità e bacini di attrazione differenti. Per quanto riguarda il flusso base asimmetrico, non tutta la fenomenologia è stata spiegata e questo lavoro si propone di fare maggior chiarezza su aspetti ancora poco indagati. In particolare, il presente studio è volto ad analizzare la stabilità del flusso base asimmetrico, al variare dei due parametri che governano la corrente, ovvero il numero di Reynolds e la distanza tra i centri dei cilindri. Infatti, alcuni autovalori che delimitano la zona di asintotica stabilità del flusso base asimmetrico all'interno dello spazio dei parametri, sembrano essere sensibili alla lunghezza del dominio, rendendo necessaria la ridefinizione della suddetta area, calcolata da Carini in [10]. Di conseguenza, gli obiettivi di questa tesi sono due:

- identificare la lunghezza minima del dominio di calcolo per la quale gli autovalori relativi alle curve neutre che delimitano il perimetro della zona stabile sono a convergenza;
- utilizzare quel dominio per ridefinire la zona di asintotica stabilità calcolata in [10];

Formulazione matematica La corrente attorno ai due cilindri affiancati è stata modellata utilizzando le equazioni di Navier–Stokes sotto l'ipotesi di flusso incomprimibile e stazionario. Dal momento che il problema di partenza è non lineare, le equazioni sono state linearizzate attorno alle diverse posizioni di equilibrio nello spazio dei parametri, in modo da poter svolgere l'analisi di stabilità lineare nei punti di interesse. Il calcolo degli autovalori del problema linearizzato è stato effettuato utilizzando l'algoritmo di Arnoldi implementato nella libreria ARPACK. La necessità di tracciare le curve neutre nello spazio (Re, g) ha richiesto l'utilizzo di un algoritmo di continuazione che consentisse il corretto inseguimento delle biforcazioni di Hopf relative a quegli autovalori marginalmente stabili che definiscono la zona stabile; l'algoritmo in questione è opportunamente interfacciato con la libreria open-source LOCA. Infine, a completamento dell'analisi, è stato effettuato un calcolo della sensitività strutturale con l'obiettivo di individuare la regione in cui fosse localizzata l'instabilità e quindi dove il flusso fosse maggiormente sensibile a una perturbazione in retroazione localizzata.
La modellazione numerica del flusso attorno ai due cilindri è stata effettuata attraverso il metodo dei corpi immersi; questo metodo prevede che la geometria attorno alla quale si vuole studiare il flusso non sia fisicamente presente all'interno del dominio di calcolo, ma venga modellata attraverso l'uso di opportune forzanti inserite nelle equazioni di governo.

Validazione Tutti i programmi utilizzati, implementati in linguaggio CPL dal Prof. Flavio Giannetti dell'Università di Salerno, sono stati opportunamente validati prendendo come caso di riferimento la corrente attorno a un cilindro isolato e mettendo a confronto i risultati ottenuti, con quelli disponibili in letteratura. In particolare, per quanto riguarda il flusso base, sono stati misurati il coefficiente di resistenza e la lunghezza della bolla di ricircolo presente dietro al cilindro, per diversi numeri di Reynolds. Il calcolo degli autovalori è stato validato stimando la posizione nel piano complesso dell'autovalore marginalmente stabile che si incontra a $Re \approx 46.6$ e comparandola con i risultati ottenuti in [12]. La sensitività strutturale è stata invece calcolata a $Re = 50$, visti i risultati ben consolidati riportati in [6]. Per quanto riguarda il tracciamento delle curve neutre si è trattato il caso cilindro isolato posto in rotazione e investito da una corrente uniforme, riproducendo con successo i risultati ottenuti da Pralits, Brandt e Giannetti in [8]. In generale tutti i software utilizzati si sono dimostrati affidabili riproducendo con fedeltà i dati di riferimento.

Flusso attorno a due cilindri affiancati L'analisi di stabilità del flusso base asimmetrico attorno a due cilindri affiancati è stata svolta in tre passi: prima di tutto si è cercato di capire per quale lunghezza del dominio di calcolo gli autovalori che delimitano la zona asintoticamente stabile fossero a convergenza. In particolare ci si è posizionati nel punto $g = 0.7$ e $Re = 68$ per studiare il cambiamento della curva rossa continua associata ad un autovalore con parte immaginaria $\mu \approx 0.40$. Le prove sono state svolte per domini con lunghezze comprese tra $L_x = 125$ e $L_x = 950$ con un passo variabile di $25 - 50$ diametri, utilizzando quattro diversi shift nell'iterazione di Arnoldi per indagare porzioni di spettro diverse ed essere quindi sicuri dell'assenza di altri autovalori critici

isolati. Per completezza, nel caso del dominio più lungo, il ramo di autovalori più vicini all'asse immaginario è stato ricostruito interamente. Come si può notare in Figura A.1, gli autovalori a frequenza $\mu \approx 0.40$ arrivano a convergenza già a partire da $L_x = 550$, mentre l'autovalore che con il dominio più corto si presentava come instabile, rientra nella zona stabile del piano immaginario, spostando quindi la posizione della relativa curva neutra.
Tuttavia, non stato possibile tracciare le curve neutre che delimitano la zona stabile nello spazio dei parametri, utilizzando solamente l'estensione $L_x = 550$: infatti, per alcune curve, il relativo autovalore non converge se si utilizza un dominio di tale lunghezza. I risultati mostrano come, per avere dati affidabili, sia richiesta un'estensione pari almeno a $L_x = 900$.

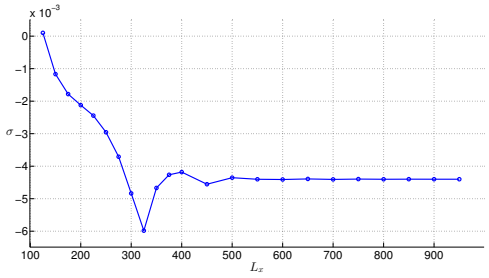

(a) $\sigma = \sigma(L_x), Re = 68, g = 0.7$.

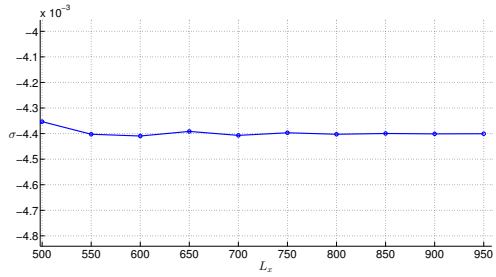

(b) *Zoom della funzione* $\sigma = \sigma(L_x), Re = 68, g = 0.7$.

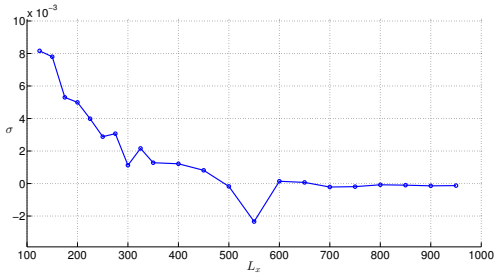

(c) $\sigma = \sigma(L_x), Re = 70, g = 0.59$.

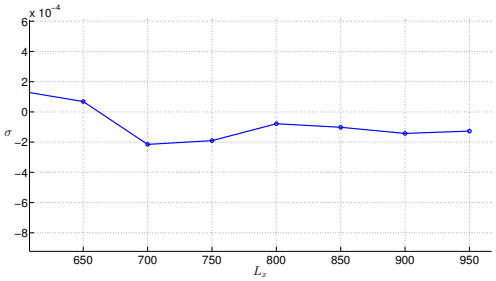

(d) *Zoom della funzione* $\sigma = \sigma(L_x), Re = 70, g = 0.59$.

Figura A.1: *Andamento della parte reale di due differenti autovalori marginalmente stabili rispetto alla lunghezza del dominio: nelle sottofigure (a) e (b) è riportato l'autovalore relativo alla curva far wake mode 5. Le sottofigure (c) e (d) mostrano l'andamento dell'autovalore corrispondente alla curva far wake mode 1.*

Una volta verificata la convergenza degli autovalori, è stata ridefinita la zona di asintotica stabilità, ricavando le nuove curve neutre con l'utilizzo dei domini allungati: come anticipato, sono stati utilizzati domini di estensione diversa. In particolare, per le curve far wake mode 1, Single Bluff Body mode e Asymmetric mode è stato impiegato il dominio piu lungo ($L_x = 950$) mentre per le altre curve è bastato utilizzare il dominio con lunghezza $L_x = 550$ visti gli ottimi risultati a convergenza, in modo da risparmiare sui

tempi di calcolo.

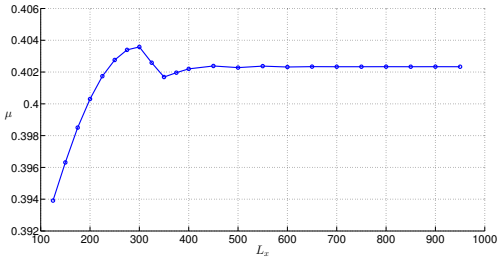

(a) $\mu = \mu(L_x), Re = 68, g = 0.7$.

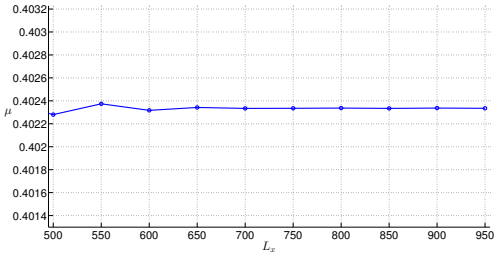

(b) *Zoom della funzione* $\mu = \mu(L_x)$, $Re = 68$, $g = 0.7$.

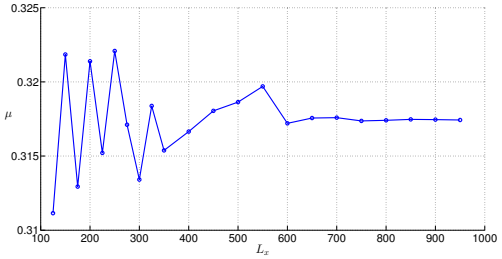

(c) $\mu = \mu(L_x), Re = 70, g = 0.59$.

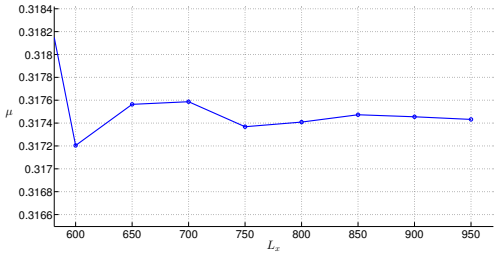

(d) *Zoom della funzione* $\mu = \mu(L_x), Re = 70, g = 0.59$.

Figura A.2: *Andamento della parte immaginaria di due differenti autovalori marginalmente stabili rispetto alla lunghezza del dominio: nelle sottofigure (a) e (b) è riportato l'autovalore relativo alla curva far wake mode 5. Le sottofigure (c) e (d) mostrano l'andamento dell'autovalore corrispondente alla curva far wake mode 1.*

Globalmente, come si può vedere in Figura A.2, l'area in cui il flusso è asintoticamente stabile si è modificata soprattutto nella sua parte sinistra, mentre nella zona di destra i risultati con domini corti erano evidentemente già molto buoni. In particolare, rispetto al grafico di partenza, la cuspide nella parte superiore dell'area stabile è sparita e la curva rossa continua si è spostata leggermente più in alto per $g < 0.9$; anche la curva far wake mode 1 ha modificato il proprio percorso, aumentando la pendenza e mostrando un cambio di curvatura in corrispondenza del punto di biforcazione di codimensione due, dove avviene l'incrocio con la curva rossa. Il tracciamento del tratto di curva far wake mode 1 compreso tra i punti $Re = 70$ e $Re = 80$ ha richiesto particolare attenzione, a causa del comportamento fortemente non lineare della curva e in relazione al fatto che nel punto di incontro tra le due curve, i rispettivi autovalori hanno una parte immaginaria molto simile tra loro, intorno a $\mu = 0.3$. Questa coincidenza manda in crisi l'algoritmo di continuazione, il quale non riesce più a stabilire quale sia il corretto autovalore da inseguire e quindi quale sia la giusta curva neutra da tracciare. Infine, anche la curva Single Bluff Body mode ha modificato il proprio andamento, inclinandosi leggermente verso sinistra e andando a chiudere l'angolo della zona stabile, nell'intorno del punto

$Re = 56$, $g = 0.546$.

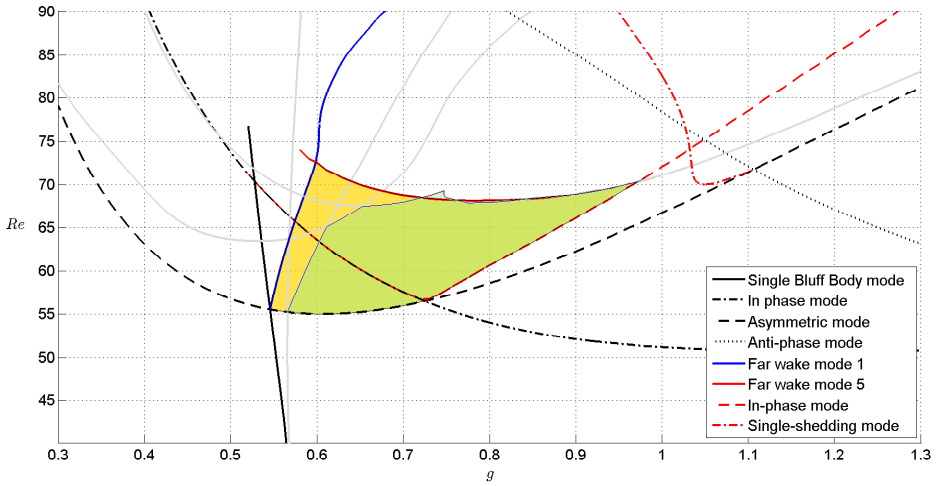

Figura A.3: *Sovrapposizione delle due aree stabili del flusso base asimmetrico nello spazio dei parametri. L'area verde è quella calcolata da Carini, mentre la zona gialla è stata ricostruita nell'ambito di questo lavoro utilizzando i domini di calcolo allungati. Le linee grigie rappresentano le vecchie curve neutre che, con l'estendersi del dominio, sono scomparse o hanno cambiato la loro posizione nello spazio dei parametri. Sono state riportate per dare una visione d'insieme su come si siano modificati i contorni dell'area stabile.*

La terza ed ultima parte del lavoro è da considerarsi una verifica del lavoro svolto, attraverso tredici simulazioni dirette, con le quali si è voluto validare i risultati precedentemente ottenuti. Per questo tipo di analisi sono stati scelti i punti nello spazio dei parametri posti a cavallo delle curve neutre che delimitano l'area stabile. L'algoritmo utilizzato si basa su uno schema temporale di tipo Crank Nicolson-Adam Bashforth 2 per velocizzare il calcolo delle quantità di interesse ad ogni istante temporale. Questo ha però richiesto però passi temporali molto piccoli, $\Delta t = 0.005$. Il tempo finale raggiunto è pari a $T = 500$. Nonostante ciò, per alcune simulazioni, l'istante finale è stato allungato a $T = 1000$ per permettere all'instabilità presente nel flusso di emergere. La condizione iniziale di ogni DNS è rappresentata dal flusso base nel punto in questione opportunamente perturbato dalla parte reale relativa all'autovalore meno stabile della curva neutra più vicina. Siccome la curva neutra far wake mode 1 è stata ricavata utilizzando una lunghezza pari a $L_x = 950$, le DNS nei punti a cavallo della suddetta curva sono state effettuate mantenendo inalterata l'estensione del dominio. Per tutti gli altri punti è stata invece utilizzata una lunghezza $L_x = 550$.
A fronte della notevole quantità di grafici relativi ai risultati delle simulazioni, si è deciso di non riportare per la seconda volta i risultati in questo Appendice, rimandando il lettore al relativo paragrafo sulle DNS presente nel Capitolo 3. Com'è possibile notare, a

fronte di una perturbazione sufficientemente piccola del flusso base, dopo un transitorio abbastanza lungo, nei punti instabili il flusso comincia ad oscillare allontanandosi dalla condizione iniziale di equilibrio, mentre nelle zone stabili la perturbazione iniziale si attenua e il flusso ritorna nella posizione iniziale.

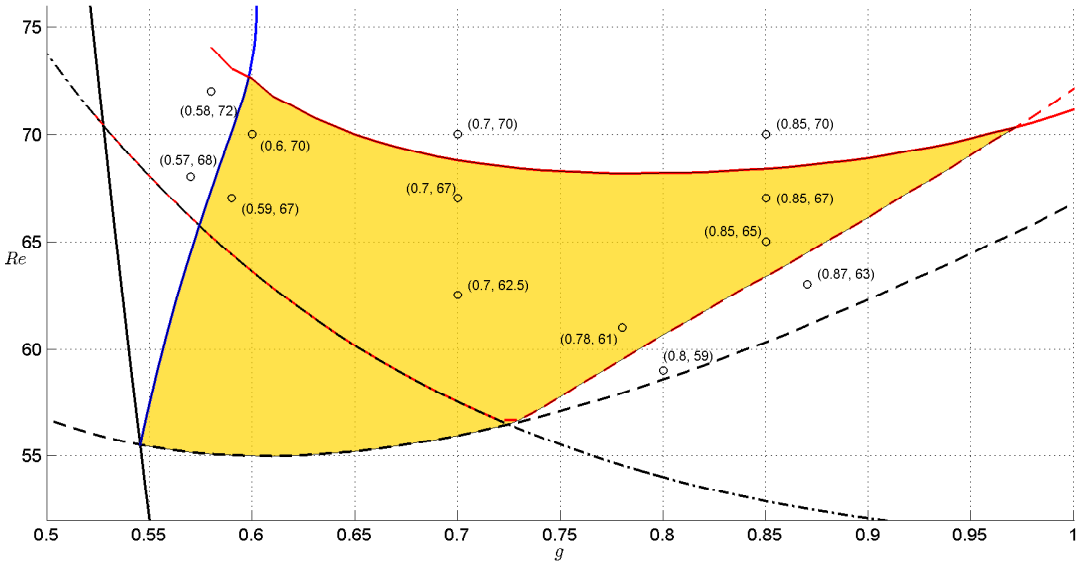

Figura A.4: *Punti nello spazio dei parametri nei quali sono state effettuate le tredici DNS.*

Bibliography

[1] P. Le Gal, M. P. Chauvre, R. Lima, J. Rezende. Coupled wakes behind two circular cylinders. *Rapid Communication*, 41: 4565-4572, 1990.

[2] S. J. Xu, Y. Zhou, M. R. C. So. Reynolds number effect on the flow structure behind two circular side-by-side cylinders. *Physics of fluids* , 5: 1214-1219, 2003.

[3] S. J. Xu, Y. Zhou, M. R. C. So. Reynolds number effect on the flow structure behind two circular side-by-side cylinders. *Physics of Fluids* , 5: 1214-1219, 2003.

[4] Sangmo Kang.Characteristics of flow over two circular cylinders in a side-by-side arrangement at low Reynolds numbers. *Physics of Fluids* , 9: 2486-2498, 2003.

[5] Takeshi Akinaga and Jiro Mizushima. Linear Stability of flow past two circular cylinders in a side-by-side arrangement. *Journal of the Physical Society of Japan*, 5: 1366-1369, 2005.

[6] F .Giannetti and P. Luchini. Structural sensitivity of the first instability of the cylinder wake. *Journal of Fluid Mechanics*, 581: 167-197, 2007.

[7] J. Mizushima and Y. Ino. Stability of flows past a pair of circular cylinders in a side-by-side arrangement. *Journal of Fluid Mechanics*, 595: 491-507, 2008.

[8] Jan O. Pralits, Luca Brandt, and Flavio Giannetti. Instability and sensitivity of the flow around a rotating circular cylinder. *Journal of Fluid Mechanics*, 1-24, 2010.

[9] M. Carini, F. Giannetti and F. Auteri. On the origin of the flip-flop instability of two side-by-side cylinder wakes. *Journal of Fluid Mechanics*, 742:552-576, 2014.

[10] M. Carini, F. Giannetti and F. Auteri. First instability and structural sensitivity of the flow past two side-by-side cylinders. *Journal of Fluid Mechanics*, 749:627-648, 2014.

[11] Ming Zhao, Liang Cheng, Bin Teng, Dongfang Liang. Numerical simulation of viscous flow past two circular cylinders of different diameters. *Applied Ocean Research*, 39-55, 2004.

[12] Denis Sipp and Anton Lebedev. Global stability of base and mean flows: a general approach and it's applications to cylinder andopen cavity flows. *Journal of Fluid Mechanics*, 593:333-358, 2007.

[13] O. Marquet, D. Sipp, L. Jacquin, J. M. Chomaz. Multiple timescale and sensitivity analysis for the passive control of the cylinder flow. *AIAA*, 1-10, 2008.

[14] O. Marquet, D. Sipp and L. Jacquin. Sensitivity analysis and passive control of cylinder flow. *Journal of Fluid Mechanics*, 615:221-252, 2008.

[15] A. F. L. Lima E Silva, A. Silveira-Neto, J.J.R. Damasceno. Numerical simulation of two-dimensional flows over a circular cylinder using the immersed boundary method. *Journal of Computational Physics*, 189:351-370, 2003.

[16] Fadlun, E. A., Verzicco, R., Orlandi, P. and Mohd-Yusof, J. Combined immersed-boundary finite-difference methods for three-dimensional complex flow simulations. *Journal of Computational Physics*, 161: 35–60,2000.

[17] Mohd-Yusof, J. Combined immersed-boundary/B-spline methods for simulations of flows in complex geometries. *Annu. Res. Briefs. Center for Turbulence Research, NASA Ames and Standford University*, p. 317, 1997.

[18] Kim, J., Kim, D. and Choi, H. An immersed-boundary finite-volume method for simulations of flow in complex geometries. *Journal of Computational Physics*, 171: 132–150, 2001.

[19] Dennis, S. R. C. and Chang, G. Numerical solutions for steady flow past a circular cylinder atReynolds number up to 100. *Journal of Fluid Mechanics*, 42, 471–489, 1970.

[20] Coutanceau, M. and Bouard, R. Experimental determination of the main features of the viscous flow in the wake of a circular cylinder in uniform translation. Part 1. Steady flow. *Journal of Fluid Mechanics*, 79: 231–256, 1977.

[21] Fornberg, B. A numerical study of steady viscous flow past a circular cylinder. *Journal of Fluid Mechanics*, 98: 819–855, 1980.

[22] Ye, T., Mittal, R., Udaykumar, H. S. and Shyy, W. An accurate Cartesian grid method for viscous incompressible flows with complex immersed boundaries. *Journal of Computational Physics*, 156: 209–240, 1999.

[23] Andrew G. Salinger, Nawaf M. Bou-Rabee, Roger P. Pawlowski, Edward D. Wilkes, Elizabeth A. Burroughs, Richard B. Lehoucq, and Louis A. Romero, *Library Of Continuation Algorithms: Theory and Implementation Manual*, 2002.

[24] Yuri A. Kuznetsov, *Elements of Applied Bifurcation Theory, Second Edition*, Springer, 2002.

[25] Schmid & Henningson, *Stability and Transition in Shear Flows*, Springer, 2001.

[26] P. Luchini & A. Bottaro. Adjoint equations in Stability Analysis, *Annual review of Fluid Mechanis*, 2014.